

Do the stellar populations of the brightest two group galaxies depend on the magnitude gap?

M. Trevisan^{1*}, G. A. Mamon¹, H. G. Khosroshahi^{1,2}

¹*Institut d'Astrophysique de Paris (UMR 7095: CNRS & UPMC, Sorbonne Universités), 98 bis Bd Arago, 75014 Paris, France*

²*School of Astronomy, Institute for Research in Fundamental Sciences (IPM), P.O. Box 19395-5531, Tehran, Iran*

Accepted —. Received —; in original form —

ABSTRACT

We investigate how the stellar populations of the inner regions of the first and the second brightest group galaxies (respectively BGGs and SBGGs) vary as a function of magnitude gap, using an SDSS-based sample of 550 groups with elliptical BGGs. The sample is complete in redshift, luminosity and for $\Delta\mathcal{M}_{12}$ up to 2.5 mag, and contains 59 large-gap groups (LGGs, with $\Delta\mathcal{M}_{12} > 2.0$ mag). We determine ages, metallicities, and SFHs of BGGs and SBGGs using the STARLIGHT code with two different single stellar population models (which lead to important disagreements in SFHs), and also compute $[\alpha/\text{Fe}]$ from spectral indices. After removing the dependence with galaxy velocity dispersion or with stellar mass, there is no correlation with magnitude gap of BGG ages, metallicities, $[\alpha/\text{Fe}]$, and SFHs. The lack of trends of BGG SFHs with magnitude gap suggests that BGGs in LGGs have undergone more mergers than those in small-gap groups, but these mergers are either dry or occurred at very high redshift, which in either case would leave no detectable imprint in their spectra. We show that SBGGs in LGGs lie significantly closer to the BGGs (in projection) than galaxies with similar stellar masses in normal groups, which appears to be a sign of the earlier entry of the former into their groups. Nevertheless, the stellar population properties of the SBGGs in LGGs are compatible with those of the general population of galaxies with similar stellar masses residing in normal groups.

Key words: galaxies: clusters: general – galaxies: elliptical and lenticular, cD – galaxies: formation – galaxies: evolution – galaxies: stellar content

1 INTRODUCTION

Galaxy groups are believed to play a key role in the formation and evolution of galaxies. There are several observational pieces of evidence suggesting that the environment where galaxies reside affects their evolution, changing their properties (Oemler 1974; Dressler 1980; Weinmann et al. 2006; Peng et al. 2010; von der Linden et al. 2010; Mahajan et al. 2011). Determining how environmental processes operate is of particular importance to understand the formation of massive elliptical galaxies, which are known to reside preferentially in the cores of groups. Gravitational phenomena such as interactions and mergers of galaxies are more frequent in high-density environments than in the field (Mamon 1992). Also, dynamical friction (Chandrasekhar 1943) dissipates orbital energy and angular momentum of the satellite galaxies, driving them to the group centre until they finally merge with the central galaxy in a few Gyr (White 1976; Schneider & Gunn 1982; Mamon 1987; Ponman et al. 1994). Therefore, the formation and evolution of the brightest galaxies in the Universe are expected to be closely linked to the growth of their host groups.

The r -band absolute magnitude gap (hereafter *magnitude gap* or simply *gap*), which we denote $\Delta\mathcal{M}_{12}$, between the group first and second-ranked galaxies, in r -band luminosity (hereafter BGG for *Brightest Group Galaxy* and SBGG for *Second Brightest Group Galaxy*), is often used as a diagnostic of past mergers among the more massive (or luminous) galaxies in groups (Ponman et al. 1994; van den Bosch et al. 2007; Dariush et al. 2010; Hearin et al. 2013).

Many studies have shown that there is a class of systems characterized by bright isolated elliptical galaxies embedded in haloes with X-ray luminosities comparable to those of an entire group. The magnitude gap observed in these systems point to a very unusual luminosity function (LF), and these objects – usually referred as *fossil groups* (hereafter FGs) – have been puzzling the astronomical community for over two decades, since their discovery by Ponman et al. (1994). Jones et al. (2003) established the first formal definition, in which a system is classified as fossil if their bolometric X-ray luminosity is greater than $L_{X,\text{bol}} \geq 10^{42} h_{50}^{-2} \text{ erg s}^{-1}$, and if they are large-gap groups (LGGs), i.e., the magnitude gap within 0.5 virial radius is $\Delta\mathcal{M}_{12} > 2$ mag (in the r -band).

The origin and nature of FGs is still matter of debate. It is not clear if the merger scenario (Carnevali et al. 1981; Mamon 1987)

* E-mail: trevisan@iap.fr

can account for groups with such large magnitude gaps, and alternative scenarios have been proposed to explain the formation of these systems. They could be “failed groups” with atypical LFs missing high-luminosity ($\approx L^*$) galaxies, while including very high ones (Mulchaey & Zabludoff 1999). Based on differences between the isophotal shapes of central galaxies located in FGs (which are often disk-like) and in normal groups (which have boxy shapes), Khosroshahi, Ponman & Jones (2006) suggested that, unlike the central galaxies of normal groups, the first-ranked galaxies in FGs were produced in a wet merger event at high redshift.

Studies of the evolution of FGs in cosmological simulations seem to suggest that the mass assembly histories of FG haloes differ from those of small luminosity gap groups (D’Onghia et al. 2005; Dariush et al. 2007; Raouf et al. 2014). A natural question is whether such a difference in the evolution of FGs is imprinted in the global properties of the stellar content and in the star formation history of the brightest group galaxies. The detailed reconstruction of the stellar assembly of galaxies is, therefore, a powerful tool to constraint different scenarios and processes taking place during the formation and evolution of these objects.

It is still not clear whether the stellar population properties of FG BGGs differ from those of BGGs located in regular groups. Several studies show that FGs have lower optical to X-ray luminosity ratios compared to regular systems (Jones et al. 2003; Yoshioka et al. 2004; Khosroshahi et al. 2007; Proctor et al. 2011), indicating that FGs have abnormally high M_{halo}/L_r at given M_{halo} (but see Voevodkin et al. 2010, Harrison et al. 2012, and Girardi et al. 2014 for an alternative view). While these results are usually interpreted as a lack of cold baryons at given halo mass, one may wonder whether part of those trends is caused by differences in the stellar population properties. If it is the case, galaxy properties that affect the M_*/L ratios, such as age and metallicity, may vary with the magnitude gap, and the high M_*/L ratios of FG BGGs could indicate that these systems are older and/or more metal-rich than those residing in normal groups.

La Barbera et al. (2009) used Sloan Digital Sky Survey Data release 4 (SDSS-DR4) and ROentgen SATellite (ROSAT) All Sky Survey X-ray data to define a sample of 25 FGs, and compared their properties with “field” galaxies selected from the same dataset. The examination of stellar populations revealed that FG BGGs have similar ages, metallicities, and α -enhancements compared to the field galaxies. More recently, Eigenthaler & Zeilinger (2013) determined the age and metallicity gradients in a sample of six BGGs in FGs from deep long-slit observations with ISIS spectrograph at the William Herschel Telescope. They found that metallicity gradients are weak ($\nabla[M/H] = -0.19 \pm 0.08$), while age gradients are negligible ($\nabla\text{age} = 0.00 \pm 0.05$), suggesting that FGs are the result of multiple major mergers. The comparison of their results with gradients in early-type galaxies determined by Koleva et al. (2011) indicates that FG BGGs follow similar ∇age , $\nabla[M/H]$ vs. stellar mass trends as regular elliptical galaxies. However, these studies suffer from low number statistics, therefore limiting their conclusions.

Finally, previous studies show that, at fixed halo mass, the stellar mass of BGGs in FGs are greater than those of their counterparts in regular groups (e.g. Díaz-Giménez et al. 2008; Harrison et al.

2012). Since galaxy properties (e.g. morphology, colour, ages, and metallicities) seem to be strongly related to stellar mass (Balogh et al. 2009; McGee et al. 2011; Trevisan et al. 2012; Woo et al. 2013), the differences between fossil and regular groups – if they exist – could be at least partially related to differences in stellar mass.

In this paper, we aim to obtain a clearer picture of the formation of the brightest galaxies and their host groups by studying how their stellar population properties and SFHs vary with the magnitude gap after correcting for the variations with the velocity dispersion, which is a proxy for the galaxy stellar mass. We use a large sample of 550 SDSS groups at $0.015 \leq z_{\text{group}} \leq 0.07$ and more massive than $\log(M_{\text{halo}}/M_{\odot}) \geq 13.1$. Our sample is complete up to $\Delta\mathcal{M}_{12} = 2.5$ mag, and contains 59 groups with $\Delta\mathcal{M}_{12} \geq 2.0$ mag.

This paper is organized as follows. In Section 2, we describe the sample of groups and the data used in our analysis. In Section 3, we investigate how the properties of groups and their brightest two galaxies vary with $\Delta\mathcal{M}_{12}$. In Section 4, we discuss the possible implications of our findings to the origin of FGs. Finally, in Section 5, we present the summary and the conclusions of our study. All masses and distances are given in physical units unless otherwise specified. To be consistent with the group catalogue used in this study, we adopt, throughout this paper, a Λ CDM cosmology with $\Omega_M = 0.238$, $\Omega_{\Lambda} = 0.762$, $\Omega_b = 0.042$ and $H_0 = 73 \text{ km s}^{-1} \text{ Mpc}^{-1}$.

2 DATA

2.1 Sample selection

The galaxy groups were selected from the updated version of the catalogue compiled by Yang et al. (2007).² The group catalogue contains 468,822 groups drawn from a sample of 593,617 galaxies from the Main Galaxy Sample (Strauss et al. 2002) of the SDSS-Data Release 7 (DR7, Abazajian et al. 2009) database and 3234 galaxies with redshift determined by alternative surveys: Two Degree Field Galaxy Redshift Survey (2dFGRS, Colless et al. 2001), Point Source Catalog Redshift Survey (PSCz, Saunders et al. 2000), and the Third Revised Catalog of Galaxies (RC3, de Vaucouleurs et al. 1991).³

The radii r_{180} , i.e. the radii of spheres that are 180 times denser than the *mean* density of the Universe, are derived from the M_{180} masses given in the Yang et al. catalogue, which are based on the ranking of Petrosian luminosities. We then calculated the virial radii ($r_{\text{vir}} = r_{200}$, where r_{200} are the radii of spheres that are 200 times denser than the *critical* density of the Universe) and masses ($M_{\text{halo}} \equiv M_{\text{vir}} = M_{200} = 100 H^2(z) r_{200}^3 / G$) by assuming the NFW (Navarro, Frenk & White 1996) profile and the concentration-mass relation given by Dutton & Macciò (2014).⁴

We selected groups that satisfy the following criteria:

- (i) redshifts in the range from 0.015 to 0.07;
- (ii) at least 5 member galaxies;
- (iii) masses $\log(M_{\text{halo}}/M_{\odot}) \geq 13.1$;

¹ Their sample was not selected from a group catalogue. The magnitude gaps of the optical FG candidates and the control sample were defined within a cylinder with radius of 350 kpc and $\Delta z = 0.001$ centered on the galaxy.

² The group catalogue is publicly available at gax.shao.ac.cn/data/Group.html.

³ This corresponds to sample2_L_petro among the Yang et al. group catalogues.

⁴ See appendix A for the conversion of Yang’s virial radii to our definition.

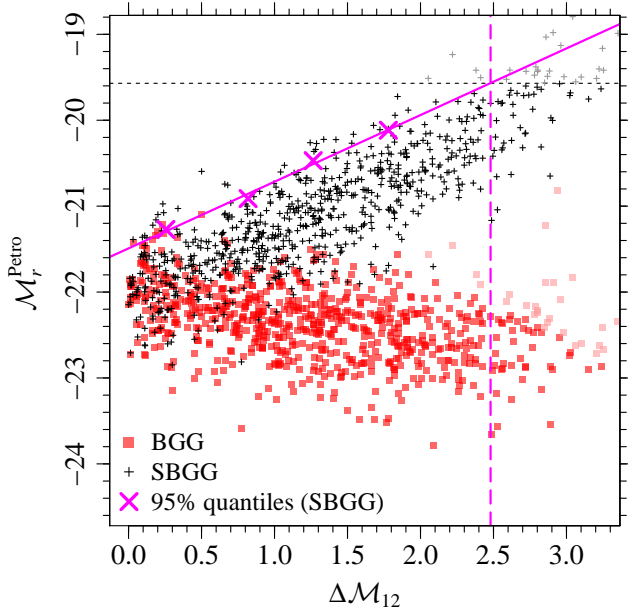


Figure 1. Luminosity versus magnitude gap diagram to extract the completeness limit for the magnitude gap of our sample. The BGGs and SBGGs are shown as red and black symbols. The solid magenta lines indicates the linear fit to the 95-percentiles of $\mathcal{M}_{r,2}^{\text{Petro}}$ in bins of $\Delta\mathcal{M}_{12}$. The 95% completeness magnitude limit of our full sample is shown as the black dashed horizontal line ($\mathcal{M}_r^{\text{Petro}} = -19.57$). Therefore, the 90 percent complete magnitude gaps for the full sample is found where the solid magenta line meets the dashed horizontal line.

(iv) at least two member galaxies within $0.5 r_{\text{vir}}$ brighter than $\mathcal{M}_r^{\text{Petro}} \leq -19.57$, where $\mathcal{M}_r^{\text{Petro}}$ is the k-corrected SDSS Petrosian absolute magnitude in the r band;

(v) the magnitude gap, defined as the difference between the k-corrected SDSS r -band Petrosian absolute magnitudes of the BGG and SBGG galaxies within half the virial radius, i.e.,

$$\Delta\mathcal{M}_{12} = \mathcal{M}_{r,2}^{\text{Petro}} - \mathcal{M}_{r,1}^{\text{Petro}},$$

is smaller than 2.47 mag;

(vi) first-ranked galaxy classified as an elliptical galaxy according to the information retrieved from Galaxy Zoo 1 project database (Lintott et al. 2011);

(vii) the relative velocity of the SBGG with respect to the BGG must be $< 2.7\sigma_{\text{los}}(R)$, where $\sigma_{\text{los}}(R)$ is the predicted line-of-sight group velocity dispersion at a distance R from the BGG.

The lower redshift limit was chosen to avoid selecting groups too close to the edge of the catalogue (the groups were defined using galaxies at $0.01 < z_{\text{gal}} < 0.2$). The upper limit was optimized to obtain the largest possible number of groups with $\Delta\mathcal{M}_{12} \geq 2$ mag, given the other criteria and taking into account the variation of $\mathcal{M}_r^{\text{Petro}}$ and $\Delta\mathcal{M}_{12}$ limits with z .

The $\log M_{\text{halo}}$, $\mathcal{M}_r^{\text{Petro}}$, and $\Delta\mathcal{M}_{12}$ completeness limits were established as follows. We compared the halo mass function of our sample with the theoretical halo mass function computed using the NUMCOSMO package⁵ (Dias Pinto Vitenti & Penna-Lima 2014).

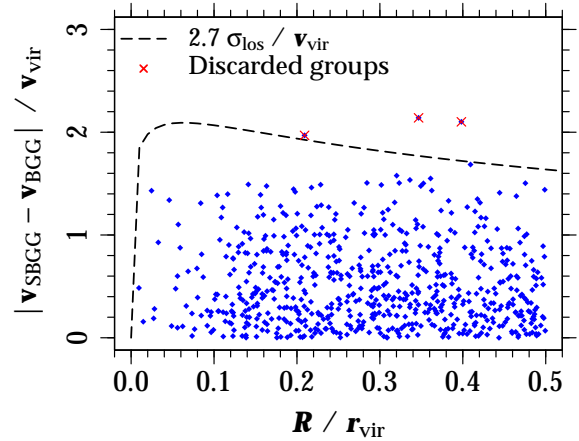


Figure 2. Distribution of SBGGs in projected phase space (line-of-sight velocity relative to the BGG versus projected distance to the BGG). The velocities and distances are normalized to the virial velocity (v_{vir} , see text) and radius (r_{vir}), respectively. The dashed line corresponds to $2.7\sigma_{\text{los}}(R)/v_{\text{vir}}$, where $\sigma_{\text{los}}(R)$ is the predicted line-of-sight velocity dispersion at a projected distance R from the BGG (see text). The groups that lie above the curve are discarded from the sample (red crosses).

The adopted halo mass lower limit, $\log(M_{\text{halo}}/M_{\odot}) \geq 13.1$, corresponds to the value above which the difference between the observed and theoretical mass functions is smaller than ~ 0.1 dex.

The sample limit in absolute magnitude cannot be simply derived from our adopted maximum redshift and the limit of extinction-corrected apparent magnitudes of the SDSS MGS (which would yield $\mathcal{M}_r^{\text{Petro}} = -19.64$), because the reference frame for the k-corrections is at $z = 0.1$ and different galaxies have slightly different k-corrections. We therefore determine the 95 percent limit in absolute magnitudes following the geometric approach similar to that described by Garilli et al. (1999) and La Barbera et al. (2010). We first determine the 95 percentile of m_r^{Petro} in bins of $\mathcal{M}_r^{\text{Petro}}$ and then perform a linear fit to the 95-percentile points, so that the value of $\mathcal{M}_r^{\text{Petro}}$ where the best-fit line intersects $m_r^{\text{Petro}} = 17.77$ defines the absolute magnitude of 95 percent completeness. This leads to a 95 percent completeness limit of $\mathcal{M}_r^{\text{Petro}} \leq -19.57$ for our sample.

This absolute magnitude limit in turns leads to a sample complete up to $\Delta\mathcal{M}_{12} = 2.47$ mag, as illustrated in Fig. 1.

Finally, the upper limit for the absolute value of the relative line-of-sight velocity between the SBGG and the BGG was adopted to avoid projection effects, as illustrated in Fig. 2 (where the virial velocity is defined with $v_{\text{vir}}^2 \equiv v_{200}^2 = G M_{200}/r_{200} = 10 H(z) r_{200}$). This predicted limit, $2.7\sigma_{\text{los}}$, was computed by assuming a single-component NFW profile of concentration $c = 6$ (the value expected for haloes with $\log(M_{\text{halo}}/M_{\odot}) \sim 13.4$), with a velocity anisotropy that varies with physical radius according to the formula of Mamon & Łokas (2005), which is a good approximation to the measured velocity anisotropy in simulated Λ CDM haloes (Mamon et al. 2010).

The criteria above lead to a sample of 657 groups. The conclusions of this work depend little on the precise values used in these selection criteria. The k-corrections were obtained with the KCORRECT code (version 4_2) of Blanton et al. (2003), choosing as reference the median redshift of the SDSS MGS ($z = 0.1$).⁶

⁵ <http://www.nongnu.org/numcosmo/>

⁶ Although the median redshift of our sample is 0.05, we kept the median

2.2 Spectroscopic incompleteness

The completeness of the SDSS spectroscopy in high-density regions is affected by the fibre collision limit, which prevents neighboring fibres from being closer than $55''$. This spectroscopic incompleteness might affect the correct identification of the BGGs and SBGGs. To address this issue, we used the SDSS photometric catalogue to identify galaxies that could be BGGs or SBGGs, but have no SDSS-DR7 spectra.

We first investigate if there are galaxies within $1 r_{\text{vir}}$ from the luminosity-weighted center of each group that are brighter than the BGG of that group. We then used the SDSS-DR12 redshifts (when available⁷) to check if the galaxy is within the redshift range of the group, i.e.,

$$|z - z_{\text{group}}| < (2.7 \sigma_{\text{group}}), \quad (1)$$

If there is no SDSS-DR12 spectrum, we discard the group. We discard 12 groups that contain galaxies brighter than the BGG with redshifts in the range given by equation (1) and 30 groups with galaxies brighter than the BGG but no spectroscopic redshifts.

Following a similar approach, we retrieved from the photometric catalogue all galaxies within $0.5 r_{\text{vir}}$ from the BGGs that are brighter than the SBGG of that group and have spectroscopic redshifts according to Eq. (1), or that do not have spectroscopic redshift available (31 and 34 objects, respectively). We discard all the 65 groups that contain galaxies that follow these criteria.

In summary, following the criteria (i) to (vii) listed in Section 2.1 but discarding a total of 107 groups with incomplete SDSS-DR7 spectroscopy we obtain our final sample of 550 groups, among which 59 have $\Delta M_{12} > 2$ mag.

2.3 Galaxy properties

The galaxy magnitudes, stellar masses, velocity dispersions, and specific star formation rates (sSFR) were retrieved from the SDSS-DR12 database⁸ (Alam et al. 2015). The match between the Yang et al. catalogue and the SDSS-DR12 sample was performed with TOPCAT⁹ (Taylor 2005) by assuming a maximum separation of $5''$ between the sky positions and a maximum difference in redshift of $\Delta z < 0.0005$ (i.e. velocity differences less than 150 km s^{-1}). The stellar masses and sSFR correspond to the estimates available in the MPA-JHU spectroscopic catalogue, and described in Brinchmann et al. (2004). We also retrieved the eClass parameter from the SDSS-DR7 database, which is based on the first two eigencoefficients from the Principal Component Analysis (PCA) of galaxy spectra (Yip et al. 2004). The eClass parameter ranges from about -0.35 to 0.5 for early- to late-type galaxies.

redshift of the SDSS MGS as the reference for the k-corrections. The difference between $\mathcal{M}_{r,\text{Petro}}^{0.1}$ and $\mathcal{M}_{r,\text{Petro}}^{0.05}$ is ~ 0.1 mag, and has no effect on the results and conclusions of our study.

⁷ The spectra of many objects that are not in SDSS-DR7 are now available in DR12. However, these objects were observed with the BOSS (Baryon Oscillation Spectroscopic Survey) spectrograph, whose fibres are smaller than those of the SDSS spectrograph ($2''$ rather than $3''$). The difference in the fibre aperture might introduce bias in our results and, for this reason, we opted for not using these new spectra in our study. Therefore, we discard the groups with incomplete SDSS-DR7 spectroscopy.

⁸ The stellar mass and sSFR estimates correspond to the parameters `lgm_tot_p50` and `specsfr_tot_p50` from the SDSS table `galSpecExtra` (Kauffmann et al. 2003; Brinchmann et al. 2004; Salim et al. 2007).

⁹ <http://www.star.bris.ac.uk/~mbt/topcat/>

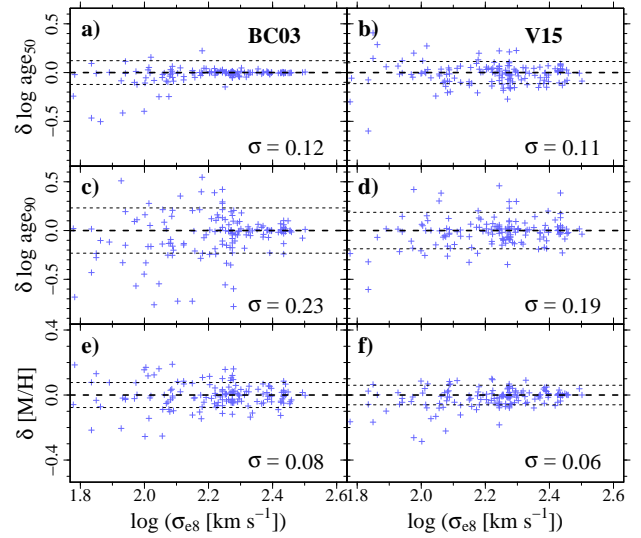


Figure 3. Uncertainties in ages and metallicities, estimated from differences between the properties derived from multiple spectroscopic observations of the same objects (δ). The left and the right panels show the results obtained with BC03 and V15 models, respectively. The long and the short dashed lines indicate $\delta = 0 \pm \sigma$, where σ is the standard deviation of the distribution of δ .

The velocity dispersions are measured through the fixed aperture of the SDSS fibre (diameter of $3''$), therefore they need to be normalized to the same physical aperture. We assume that the velocity dispersion profile is well described by $\sigma_{\text{ap}} = \sigma_{\text{e8}} [R_{\text{ap}} / (R_{\text{e}}/8)]^{-0.066}$ (Cappellari et al. 2006), where R_{e} is the effective radius of the galaxy (containing half the projected luminosity) and normalize the velocity dispersions to σ_{e8} , which corresponds to the dispersion measured through an aperture with a radius of one eighth of the effective radius.

2.3.1 Star formation histories and metallicities

We derived ages and metallicities from the SDSS spectra using the STARLIGHT spectral fitting code (Cid Fernandes et al. 2005). For each galaxy, STARLIGHT combines single stellar population (SSP) model spectra of given age and metallicity and returns the contribution, as a percentage of mass, from each basis SSP. This distribution traces directly the SFH. For each galaxy in the sample, we determine the “cumulative” mass fraction, i.e., the fraction of stars older than a given age, as a function of age. We then interpolate the cumulative SFH of each galaxy to obtain the galaxies ages, defined as the age when half of the stellar mass was already formed (i.e., $\text{age} \equiv \text{age}_{50}$), and the age when 90% of the stellar mass was formed (age_{90}). From the STARLIGHT results, we also compute the mass-weighted metallicities.

To check the dependency of the stellar population properties with the models used, we selected two sets of SSP models. One of them is based on the Medium resolution Isaac Newton Telescope Library of Empirical Spectra (MILES, Sánchez-Blázquez et al. 2006), using the updated version 10.0 (Vazdekis et al. 2015, hereafter V15) of the code presented in Vazdekis et al. (2010). We selected models computed with Kroupa (2001) universal initial mass function (IMF), and isochrones from BaSTI (Bag of Stellar Tracks and Isochrones, Pietrinferni et al. 2004, 2006).

We also used (Bruzual & Charlot 2003, BC03) models, calculated with Padova 1994 evolutionary tracks (Bressan et al. 1993; Fagotto et al. 1994a,b; Girardi et al. 1996) and with the Chabrier (2003) IMF. The BC03 model employs the STELIB stellar library (Le Borgne et al. 2003). For both sets of models, we adopted a constant log age step of 0.2, and the grids cover ages from 0.03 to 13.5 Gyr. For the BC03 models, we selected SSPs with metallicities $[M/H] = \{-1.7, -0.7, -0.4, 0.00, +0.40\}$ and the grid of V15 models contains SSPs with $[M/H] = \{-1.26, -0.66, -0.25, +0.06, +0.15, +0.40\}$.

The fit was performed in the wavelength region from 3800 to 7400 Å. Before running the code, the observed spectra are corrected for foreground extinction and de-redshifted, and the SSP models are degraded to match the wavelength-dependent resolution of the SDSS spectra, as described in La Barbera et al. (2010) and Trevisan et al. (2012). We adopted the Cardelli, Clayton & Mathis (1989) extinction law, assuming $R_V = 3.1$.

To estimate the uncertainties in the stellar population properties, we retrieved from the SDSS database all objects in our sample that have multiple spectroscopic observations. We found 168 galaxies, 62 of them being elliptical, with multiple spectra with signal-to-noise (S/N) ratio greater than 5.

In Fig. 3, we show the differences between the properties derived from multiple spectroscopic observations as a function of velocity dispersion for galaxies of all morphological types. After dividing the values of σ shown in Fig. 3 by $\sqrt{2}$, we find that the typical errors in $\log \text{age}_{50}$, $\log \text{age}_{90}$, and $[M/H]$ are 0.08, 0.16, and 0.06 (BC03), and 0.08, 0.13, and 0.04 (V15). If we consider only elliptical galaxies, whose spectra tend to have higher S/N ratios, the typical uncertainties (in dex) are 1.2 to 3 times smaller:

$$\begin{aligned} \sigma(\text{age}_{50}, \text{age}_{90}, [M/H])_{\text{E}} &= (0.03, 0.10, 0.04) \quad (\text{BC03}), \\ &= (0.06, 0.08, 0.04) \quad (\text{V15}). \end{aligned}$$

2.3.2 $[\alpha/\text{Fe}]$ ratios

The α -elements (O, Mg, Si, S, Ca, Ti) are synthesized primarily in supernovae (SN) type II (e.g. Arnett 1978, Woosley & Weaver 1995), while SNs Ia yield mostly iron-peak elements with little α -element production (e.g. Nomoto et al 1984, Thielmann et al 1986). Since SN Ia events are delayed relative to SNs II¹⁰, the $[\alpha/\text{Fe}]$ ratios are believed to be closely related to the star-formation timescales of galaxies (Tinsley 1979; Thomas et al. 2005; de La Rosa et al. 2011; Walcher et al. 2015).

To estimate the $[\alpha/\text{Fe}]$ ratios of our BGGs and elliptical SBGGs, we adopted the approach described in La Barbera et al. (2013) and Vazdekis et al. (2015), which is based on the spectral indices Mgb and Fe3¹¹. We measured the line-strengths with the INDEXF¹² code (Cardiel 2010), and applied corrections for the broadening due to the internal velocity dispersion of the galaxy following the prescriptions of de la Rosa et al. (2007).

The procedure to determine the proxy of $[\alpha/\text{Fe}]$ is illustrated in Fig. 4, where we show the BGG and the SBGG luminosity-weighted ages (derived using STARLIGHT with V15 models, see Section 2.3.1) as a function of Mgb and Fe3, as well as the

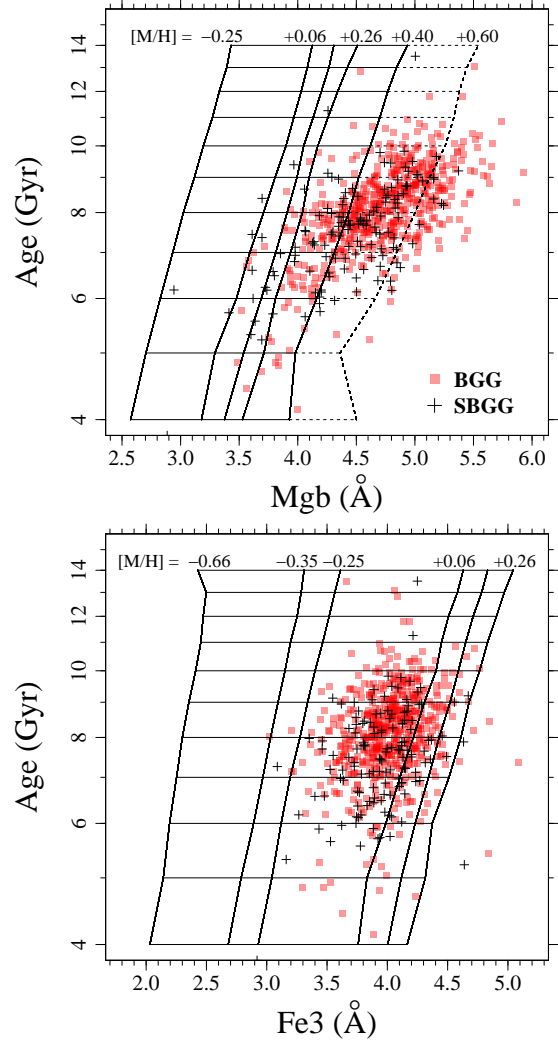


Figure 4. Illustration of the procedure to obtain the $[\alpha/\text{Fe}]$ proxy. The luminosity-weighted ages obtained using STARLIGHT with V15 models are shown as a function of the spectral indices Mgb (upper panel) and Fe3 (lower panel). The BGGs and the SBGGs are represented by the red and the black symbols, respectively, and the V15 model grids are indicated in both panels. The dashed part of the grid in the upper panel indicates our linear extrapolation of the model Mgb to $[M/H] = +0.6$.

predictions from the V15 models with different metallicities. For each galaxy, we estimate two independent metallicities, Z_{Mgb} and Z_{Fe3} , by fixing the galaxy age and interpolating the model grid. As discussed by La Barbera et al. (2013), estimating Z_{Mgb} of an α -enhanced population may require extrapolation of the models to higher metallicities. This is illustrated in the upper panel of Fig. 4, where we show our linear extrapolation of the model Mgb to metallicity $[M/H] = +0.6$. To reduce the uncertainties in the interpolated and extrapolated values, the model grids include all metallicities ≥ -0.66 available for the V15 models, i.e., $[M/H] = \{-0.66, -0.35, -0.25, +0.06, +0.15, +0.26, +0.40\}$. Finally, the proxy of $[\alpha/\text{Fe}]$ is then defined as the difference between these two metallicities, $[Z_{\text{Mgb}}/Z_{\text{Fe3}}] = Z_{\text{Mgb}} - Z_{\text{Fe3}}$.

We also computed $[\alpha/\text{Fe}]$ by taking the $[\alpha/\text{Fe}]$ ratios explic-

¹⁰ For typical elliptical galaxies, the peak of SN Ia rates occur $\sim 0.1 - 1$ Gyr later than that of SN II rates (see e.g. Matteucci & Tornambe 1987; Thomas et al. 1999; Matteucci & Recchi 2001).

¹¹ $\text{Fe3} = (\text{Fe4383} + \text{Fe5270} + \text{Fe5335})/3$ (Kuntschner 2000)

¹² <http://pendientedemigracion.ucm.es/info/Astrof/ellipt/pages/page4.html>

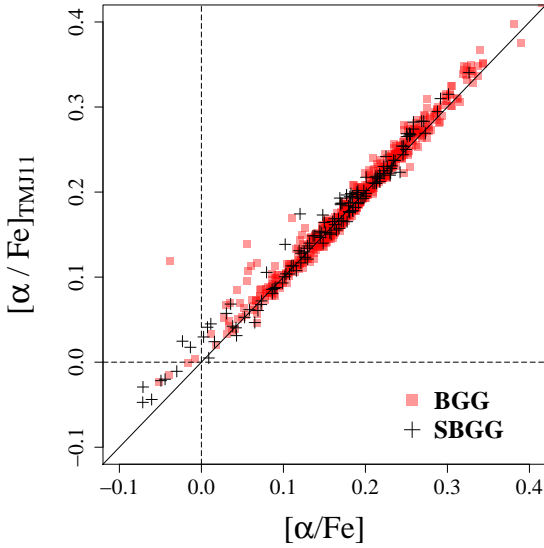


Figure 5. The $[\alpha/\text{Fe}]$ ratios estimated with Thomas et al. (2011, TMJ11) models as a function of $[\alpha/\text{Fe}]$ obtained with the V15 models. The latter corresponds to the proxy $[Z_{\text{Mgb}}/Z_{\text{Fe3}}]$ calibrated according to $[\alpha/\text{Fe}] = -0.07 + 0.51 [Z_{\text{Mgb}}/Z_{\text{Fe3}}]$ (Eq. 2).

itly into account. To this event, we compared the $[\text{Mg}/\text{Fe}]'$ ¹³, Mgb, and Fe3 indices to the predictions by Thomas et al. (2011, hereafter TMJ11). First, we estimate the metallicity $[\text{M}/\text{H}]_{\text{TMJ}}$ from the $[\text{Mg}/\text{Fe}]'$ indice, which is independent of $[\alpha/\text{Fe}]$ (Thomas et al. 2003; see also Vazdekis et al. 2015), by fixing the galaxy age and interpolating the TMJ11 model grid (i.e., we applied same procedure as illustrated in Fig. 4, but using $[\text{Mg}/\text{Fe}]'$ and different models). We then fitted the models to obtain the predicted (polynomial) relation $[\alpha/\text{Fe}] = \tilde{p}(\text{Mgb}, \text{Fe3}, [\text{M}/\text{H}], \text{age})$, and used this relation with STARLIGHT ages and $[\text{M}/\text{H}]_{\text{TMJ}}$ to obtain the $[\alpha/\text{Fe}]_{\text{TMJ11}}$ estimates. As in the previous studies by La Barbera et al. (2013) and Vazdekis et al. (2015), we find a very tight correlation between $[\alpha/\text{Fe}]_{\text{TMJ11}}$ and $[Z_{\text{Mgb}}/Z_{\text{Fe3}}]$. Selecting all elliptical galaxies within $0.5 r_{\text{vir}}$ in our sample to fit the relation between these two quantities, we find

$$[\alpha/\text{Fe}]_{\text{TMJ11}} = -0.07 + 0.51 [Z_{\text{Mgb}}/Z_{\text{Fe3}}], \quad (2)$$

with a very small scatter of 0.019 dex. If we consider only the BGGs and elliptical SBGGs, we obtain an even smaller scatter of 0.017 dex. Finally, in Fig. 5 we compare $[\alpha/\text{Fe}]_{\text{TMJ11}}$ with our final values of $[\alpha/\text{Fe}]$, i.e., the proxy $[Z_{\text{Mgb}}/Z_{\text{Fe3}}]$ calibrated according to Eq. 2.

2.4 Stellar population properties vs. velocity dispersion relations

Many studies suggest that the properties of elliptical galaxies are more correlated to velocity dispersions than to stellar masses (e.g. Bernardi et al. 2003; La Barbera et al. 2014). In addition, the uncertainties on $\log \sigma_{\text{e8}}$, as listed in the SDSS database, are typically 0.1 dex, while the errors on stellar masses are 0.2 dex (e.g. Duarte & Mamon 2015). Therefore, we analyse how the properties of the

BGGs and the elliptical SBGGs vary with $\Delta \mathcal{M}_{12}$ (see Section 3.2) after correcting the relations with $\log \sigma_{\text{e8}}$ instead of stellar masses.

To fit the relations between galaxy properties and $\log \sigma_{\text{e8}}$, we selected all elliptical galaxies within $0.5 r_{\text{vir}}$ in our sample groups and divided them in bins of $\log \sigma_{\text{e8}}$, with ~ 100 galaxies per bin. We adopt a non-parametric approach by computing the median values of the distributions of the galaxy properties in each bin and fitting these values using the locally-weighted polynomial regression method (LOESS). The relations were fit using the R function `loess`¹⁴ (R Core Team 2015). The fit is performed locally using the data points in the neighbourhood of x , weighted by their distance from x . The neighbourhood includes a proportion γ of all the points; we adopted $\gamma = 1$, i.e., all points. A 2nd-order polynomial is then fit using weighted least squares, and each data point i receives the weight proportional to $\left(1 - [d_i/\max(\vec{d})]^3\right)^3$, where d_i is the distance of the data point i to x and $\max(\vec{d})$ is the maximum distance among the data points in the neighbourhood of x .

The fitted relations are shown in Fig. 6. Some properties such as ages and sSFR show a large scatter at low velocity dispersions. To estimate how the scatter varies with $\log \sigma_{\text{e8}}$, we also computed the 16th and the 84th percentiles, q_{16} and q_{84} , of the distributions in bins of velocity dispersion and fitted the percentiles versus $\log \sigma_{\text{e8}}$ relations using the same approach described above.

For each galaxy, we then computed the normalized distance to the best fit:

$$\delta P = \frac{P - f_P(\log \sigma_{\text{e8}})}{\text{IPR}_P(\log \sigma_{\text{e8}})}, \quad (3)$$

where $f_P(\log \sigma_{\text{e8}})$ is the best fit to the relation between the median value of the galaxy property P and $\log \sigma_{\text{e8}}$, and IPR_P is the “inter-percentile” range of the distribution of the property P for galaxies with a given velocity dispersion, defined as:

$$\begin{aligned} \text{IPR}_P(\log \sigma_{\text{e8}}) &= f_P(\log \sigma_{\text{e8}}) - q_{16}(\log \sigma_{\text{e8}}), & \delta P < 0 \\ \text{IPR}_P(\log \sigma_{\text{e8}}) &= q_{84}(\log \sigma_{\text{e8}}) - f_P(\log \sigma_{\text{e8}}), & \delta P > 0 \end{aligned}$$

The errors in the fitted relations were estimated by bootstrapping the full sample 1000 times, and the 95% confidence intervals are shown as shaded areas in Fig. 6.

2.5 Differences in the star formation histories according to the single stellar population model

The star formation histories of the BC03 and V15 models turn out to be strikingly different for elliptical galaxies, as seen in Fig. 6: in comparison with the BC03 model, elliptical galaxies (within half the virial radius of their groups) with the V15 model have formed half of their stellar masses at lower redshifts. While with BC03, elliptical galaxies were formed very quickly, with 50% of their total stellar masses already formed 12 Gyr ago (Fig. 6e), with V15, 50% of the stellar mass is formed from ~ 8 to 11 Gyr ago, depending on their velocity dispersion (Fig. 6i). These differences are also clearly seen in $\log \text{age}_{90}$ (compare Figs. 6f and 6j) and in the durations of star formation (compare Figs. 6g and 6k). In addition, according to V15 models, galaxies with $\log [\sigma_{\text{e8}}/(\text{km s}^{-1})] \sim 2.4$ have metallicities that are ~ 0.2 dex higher than the values obtained with BC03 models (Figs. 6h,l).

¹³ $[\text{Mg}/\text{Fe}]' = \sqrt{\text{Mgb}(0.72 \text{ Fe5270} + 0.28 \text{ Fe5335})}$ (Thomas et al. 2003)

¹⁴ <https://stat.ethz.ch/R-manual/R-patched/library/stats/html/loess.html>

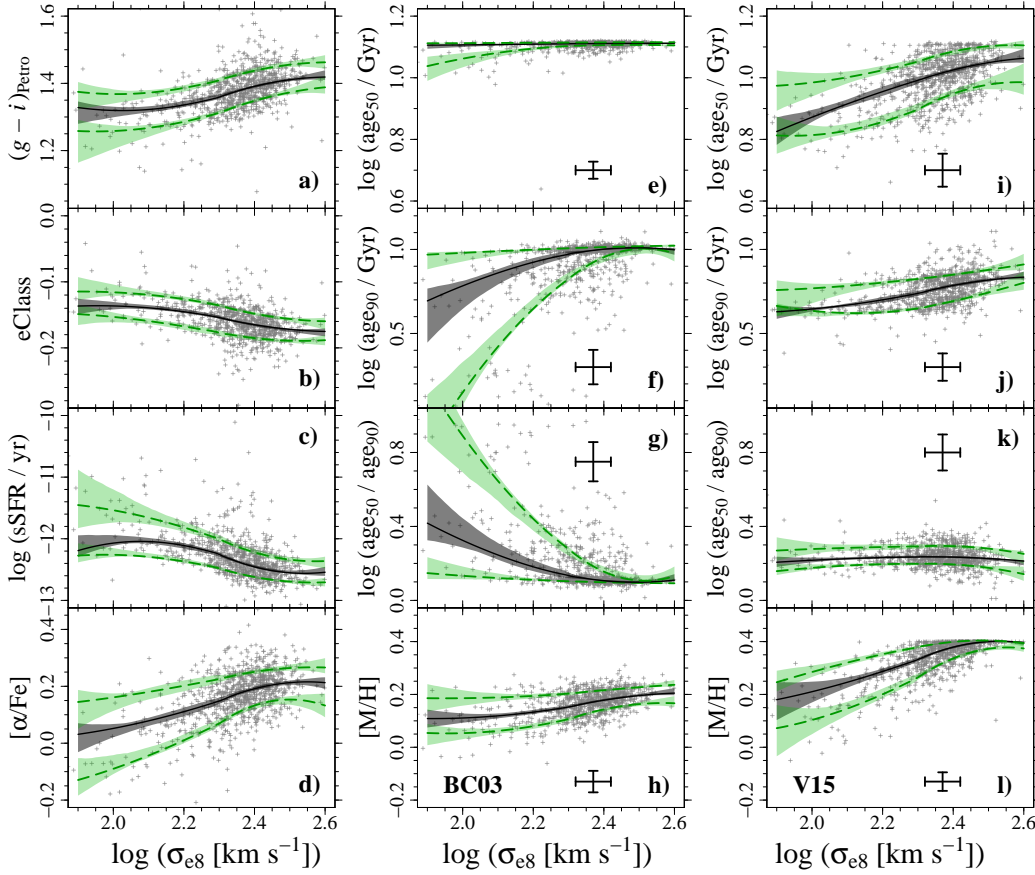


Figure 6. Galaxy properties as a function of velocity dispersion normalized to an aperture with one-eighth of the effective radius. The *left panels (a–d)* present the extinction- and k-corrected $g - i$ colour, the parameter $eClass$, the specific star formation rate, and $[\alpha/Fe]$ as a function of the $\log \sigma_{e8}$. The *middle and right panels* show the median ages ($\log age_{50}$), the lookback times at which 90% of the galaxy stellar mass was formed ($\log age_{90}$), and metallicities obtained with BC03 (panels **e–h**) and V15 (**i–l**) models. All the elliptical galaxies within $0.5 r_{vir}$ of our sample of groups are shown (*black symbols*). Typical errors in ages and metallicities are indicated in panels **e** to **l** (see Section 2.3.1). The *black solid* and the *green lines* indicate the median, the 16, and the 84 percentiles of the galaxy properties in bins of velocity dispersion. The uncertainties in the relations are indicated as *shaded areas* (95% confidence interval).

3 RESULTS

3.1 Stellar masses and velocity dispersions of BGGs and SBGGs in groups with large and small gaps

In Fig. 7, we compare the stellar masses and velocity dispersions of BGGs and SBGGs residing in groups with large (> 2 mag, 59 groups) and small (< 0.3 mag, 74 groups) magnitude gaps. For simplicity, we refer to groups with $\Delta M_{12} > 2$ and < 0.3 as *large-gap* (LGG) and *small-gap* groups (SGGs), respectively. At fixed halo mass, the stellar masses of BGGs in LGGs are ~ 0.2 dex greater than those of their counterparts in groups with small gaps (Fig. 7a), as previously noted by Díaz-Giménez et al. (2008) and Harrison et al. (2012). By construction, SBGGs in large-gap and small-gap groups have different $\log M_*$ distribution; the difference in stellar masses is ~ 0.6 dex in haloes with $\log(M_{halo}/M_\odot) \sim 13.5$ and ~ 0.8 dex for $\log(M_{halo}/M_\odot) \sim 13.1$ (Fig. 7b). Nevertheless, the $\log M_*$ versus $\log M_{halo}$ relations of BGGs and SBGGs in large-gap groups have slopes similar to that of their counterparts in SGGs. We fitted the $M_* \propto M_{halo}^\alpha$ relation and found $\alpha = 0.44 \pm 0.06$ and 0.39 ± 0.05 for BGGs in LGGs and SGGs, respectively. For the SBGGs, we get $\alpha = 0.51 \pm 0.11$ in LGGs and $\alpha = 0.38 \pm 0.05$ in SGGs.

On the other hand, BGGs in large-gap and in small-gap groups follow slightly different $M_* - \sigma_{e8}$ relations, as presented in Fig. 7c. Assuming that $M_* \propto \sigma_{e8}^\beta$, we obtain $\beta = 4.78 \pm 0.06$ for all BGGs in our sample, $\beta = 3.95 \pm 0.16$ for BGGs in SGGs, and a slightly steeper relation with $\beta = 5.61 \pm 0.26$ for BGGs in large-gap groups. Finally, we find that the slope of the SBGG $M_* - \sigma_{e8}$ relation is smaller than that of the BGG relation ($\beta = 4.30 \pm 0.08$, Fig. 7d).

3.2 Stellar populations and star formation histories versus magnitude gap

To explore the variations of the stellar population properties of elliptical BGGs and SBGGs with ΔM_{12} , we first correct the dependency of these properties with the galaxy velocity dispersion, as described in Section 2.4. In Fig. 8, we present the extinction- and k-corrected galaxy $g - i$ colour, the $eClass$ parameter, the sSFR, and $[\alpha/Fe]$ values of the BGGs and elliptical SBGGs as a function of $\log \sigma_{e8}$ (panels a–d). The figure also shows (in panels e–h for the BGGs and i–l for the SBGGs) the residuals δP (eq. [3]) of these properties as a function of magnitude gap. In each panel, we show the Kendall and Spearman correlation coefficients. We re-

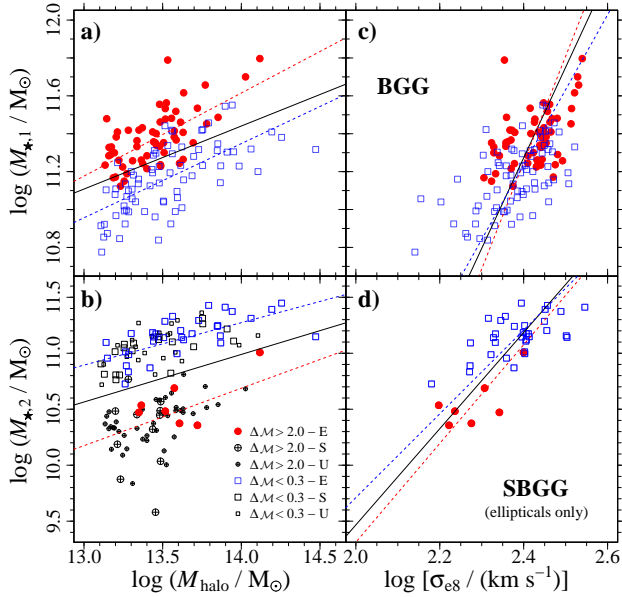


Figure 7. Stellar mass as a function of halo mass (*left panels*) and velocity dispersion (*right panels*) for the BGGs (*upper panels*) and SBGGs (*lower panels*) of groups with large ($\Delta M_{12} > 2.0$) and small ($\Delta M_{12} < 0.3$) magnitude gaps (respectively *red dots* and *blue open squares*). In panel (b), we indicate the Galaxy Zoo morphologies of the SBGGs by different symbols: elliptical (E), spiral (S), and galaxies with uncertain classification (U). The *black solid lines* shown in all panels are the best linear fits to the $\log M_*$ vs. $\log M_{\text{halo}}$ (panels a,b) and $\log M_*$ vs. $\log \sigma_{\text{e8}}$ (c,d) relations for all BGGs (a,c) or SBGGs (b,d) in our sample. The *red and blue dashed lines* are the best fits for galaxies in groups with $\Delta M_{12} > 2.0$ and < 0.3 , respectively.

peated the same procedure for stellar ages, metallicities, $\log \text{age}_{90}$, and $\log(\text{age}_{50}/\text{age}_{90})$, as shown in Figs. 9 (BC03) and 10 (V15).

Once we correct for the trend with velocity dispersion, the BGGs and SBGGs appear to share the same properties regardless of the magnitude gap of the group where they reside. The statistical tests indicate that there is no significant trend of σ_{e8} -corrected properties with ΔM_{12} for all the galaxy properties analysed (Figs. 8 to 10, panels e–l), except for the positive trend of SBGG sSFRs with gap ($\tau = 0.13$, $\rho = 0.19$, $p = 0.02$, Fig. 8k). However, this trend appear to be a consequence of galaxies having different fractions of light within the SDSS fibre, as we discuss in the next Section.

3.2.1 Aperture effects

All the quantities derived from SDSS spectra are affected by the small aperture (diameter = $3''$) of the fibre, which encompass only the inner part of the observed galaxy. As discussed by several authors (e.g. Brinchmann et al. 2004; Salim et al. 2007; Guidi et al. 2015), the presence of age and metallicity gradients (Koleva et al. 2011; Pilkington et al. 2012; La Barbera et al. 2012; Eigenthaler & Zeilinger 2013; Hirschmann et al. 2015; Sánchez et al. 2015) can lead to biases and large uncertainties in the physical properties derived from the spectra. Although bright elliptical galaxies appear to have relatively flat age, metallicity, and colour gradients (Koleva et al. 2011; La Barbera et al. 2012; Eigenthaler & Zeilinger 2013), we investigate how our results are affected by aperture effects.

We computed the fraction of Petrosian r -band light within the fibre as $f_L = \text{dex}[-0.4(m_r^{\text{fibre}} - m_r^{\text{Petro}})]$, where m_r^{fibre} and m_r^{Petro} are the fibre and Petrosian magnitudes in r -band. The maximum value of f_L among the BGGs is 33%, and 99% of our BGG sample have less than 28% of the light within the fibre. On the other hand, the SDSS spectra of SBGGs contains a larger fraction of the galaxy total luminosity, with values of f_L varying from 6 up to 42% (for elliptical SBGGs). We, therefore, investigate if our results are affected by aperture effects by repeating the analysis for galaxies with similar values of f_L . Since the range of f_L among the BGGs and the SBGGs is very different, we define different ranges of f_L to select the subsamples of BGGs and SBGGs, as we describe below.

In Fig. 11 we show how the fraction of light within the fibre varies as a function of ΔM_{12} . We indicate the 5th and 95th percentiles of the distribution of f_L in bins of gap for the BGGs and the SBGGs. For the BGGs, f_L decreases with increasing ΔM_{12} , and 95 percent of the BGGs in LGGs have $f_L < 0.20$. On the other hand, the 5th (95th) percentiles of the SBGG f_L distributions in bins of ΔM_{12} increases from 0.08 (0.30) for SBGGs in groups with $\Delta M_{12} < 0.3$ to 0.20 (0.41) in LGGs.

Therefore, to avoid selection effects when defining the subsamples of BGGs and SBGGs with similar f_L , we require that the f_L limits are within the 5th and 95th of the distribution of f_L in bins of ΔM_{12} , as illustrated in Fig. 11. We then define a subsample of 368 BGGs with $10\% < f_L < 20\%$ and another subsample of 63 elliptical SBGGs with $20\% < f_L < 30\%$, as shown in Fig. 11.

Following the approach presented in Section 2.4, we fitted the galaxy properties vs. velocity dispersion relations of all elliptical galaxies that lie within $0.5 r_{\text{vir}}$ from the BGG and have $10\% < f_L < 20\%$ (463 objects). We repeated the procedure for a sample with $20\% < f_L < 30\%$ (220 galaxies). The normalized distance to the best fit is computed using Eq. (3), and the results are presented in Tables 1 (BGGs) and 2 (SBGGs).

The correlation coefficients obtained for the BGGs with similar f_L are very similar to the ones obtained for the whole sample, with no statistically significant trend with gap of any of the properties. On the other hand, the positive trend of sSFR with gap obtained for the whole sample of elliptical SBGGs (Fig. 8k) is no longer observed when we restrict the analysis to SBGGs with similar values of f_L , indicating that this trend might be due to aperture effects.

3.3 Second-ranked galaxies in large-gap groups

The distribution of masses, magnitudes, and morphological types of SBGGs in large-gap and in small-gap groups are very different, which makes the comparison between these galaxies very difficult. The fraction of elliptical galaxies among SBGGs in LGGs is smaller than in SGGs (12% and 45%, respectively), with Barnard's test indicating high statistical significance ($p < 10^{-4}$). In Section 3.2, we focused on the variations of the elliptical SBGG properties with $\mathcal{M}_r^{\text{Petro}}$, since galaxy properties versus stellar mass relations of other morphological types have large scatter and are not as well defined as those of elliptical galaxies. Therefore, correcting the trends of properties with $\log \sigma_{\text{e8}}$ (or $\log M_*$) for galaxies other than ellipticals is not straightforward.

To overcome this issue and address the question whether LGG SBGGs of other morphological types have any peculiar property, we built a control sample of galaxies with similar stellar masses and magnitudes as the general population of galaxies residing in groups with $\Delta M_{12} < 2.0$ mag by applying the Propensity Score

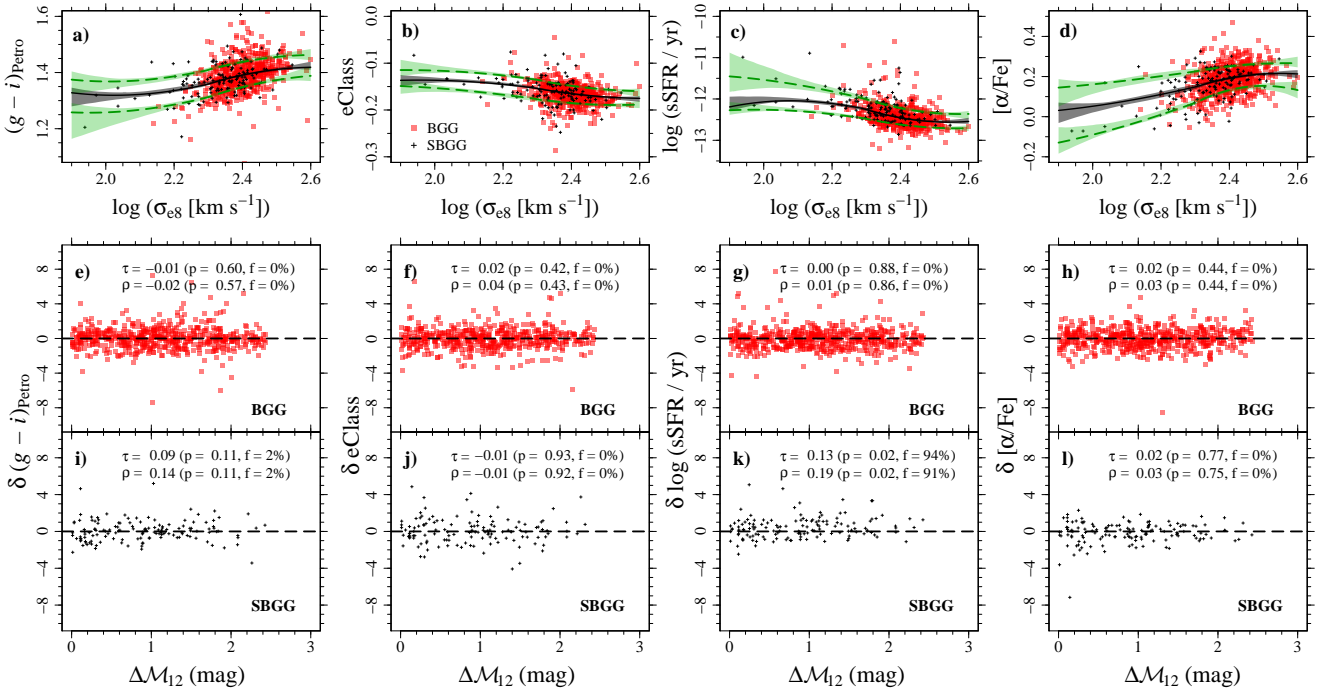


Figure 8. Galaxy properties as a function of the magnitude gap. The upper panels (a–d) present the extinction- and k-corrected $g - i$ colour, the parameter $eClass$, the specific star formation rate, and $[\alpha/Fe]$ as a function of the $\log \sigma_{e8}$. The first and the second-ranked galaxies are represented by the red and black symbols, respectively. The solid lines indicate the best fit to the properties vs. velocity dispersion relations from Fig. 6, and the green dashed lines correspond to the best fit to the 16th and 84th percentiles of the distribution in bins of $\log \sigma_{e8}$. The uncertainties in the fitted relations are shown as the grey and green shaded areas (see Sect. 2.4). The lower panels show the difference between first (e–h) and second-ranked (i–l) galaxy properties and the corresponding best-fit relation, normalized by the difference between the median and the 16th percentile (if $\delta < 0$) or the 84th percentile and the median (if $\delta > 0$, Equation 3). In each panel, we indicate the Kendall (τ) and Spearman (ρ) rank correlation coefficients, the p -values, and the fraction (f) of the 1000 realizations of the fit (see Section 2.4) that leads to $p < 0.05$.

Matching (PSM) technique (Rosenbaum & Rubin 1983). We used the MATCHIT package (Ho et al. 2011) written in R¹⁵ (R Core Team 2015). This technique allows us to select from the sample of galaxies in groups with $\Delta M_{12} < 2.0$ mag a control sample in which the distribution of observed properties is as similar as possible to that of the SBGGs in LGGs. We adopted the logistic regression approach (see e.g. Hilbe 2009; de Souza et al. 2015) to compute the propensity scores and the nearest-neighbour method to perform the matching (see details in appendix B).

As we discuss in appendix B, LGGs are typically less massive than SGGs. We therefore limit our comparison to SBGGs residing in groups with $\log(M_{halo}/M_{\odot}) < 13.7$. The control sample was selected among all satellite galaxies (i.e., rank ≥ 2) within $0.5 r_{vir}$, with $v_{los} < 2.7\sigma_v(R)$ (see Fig. 2), in groups with $\Delta M_{12} \leq 2.0$ mag and $13.1 \leq \log(M_{halo}/M_{\odot}) \leq 13.7$.

Figure 12 shows the distribution of absolute magnitudes, stellar masses and halo masses of the control sample before and after the PSM. We performed the matching by stellar mass¹⁶, and Fig. 12a illustrates the similarity of the distributions of stellar mass of the SBGGs and the control samples, as expected by construc-

tion. The distributions of SBGG absolute magnitudes and halo masses are compatible with those of the control sample, as shown in Fig. 12b,c. The sample of SBGGs in LGGs have a smaller fraction of spirals (20.8% of the LGG SBGGs and 25.5% of the control sample), and more ellipticals (9.4 and 8.4 percent) and galaxies with uncertain morphological classification (69.8 and 65.1 percent) than the control sample.

As discussed in Section 3.2.1 and shown in Fig. 11, the fixed aperture of the SDSS fibre might introduce biases in our results. However, the f_L distributions of the LGG SBGGs and of the control sample are very similar, as indicated by a KS test ($p = 0.7$), and also by differences between their median values ($\Delta = 2.05\%$) and the quantile-quantile distances ($Q - Q = 1.5\%$, see Table 3).

In Figure 13, we compare the properties of the SBGGs in LGGs with those of the control sample. We applied the KS test as a comparison diagnostic, and we indicate the resulting p -value in each panel. No clear distinction between the distributions of galaxy properties can be observed, with all p -values being greater than 0.1.

In Fig. 14a, we revisit the projected phase space diagram of SBGGs (see Fig. 2) to distinguish LGGs from the control sample. While the distribution of normalized line-of-sight velocities of the SBGGs in LGGs resembles the corresponding distribution for the control sample, there appears to be an excess of LGGs whose SBGGs lie closer to the BGG than $\sim 0.25 r_{vir}$. This appears more evident in Fig. 14b, which shows that the radial distributions (in virial units) of LGG SBGGs is shifted to smaller distances com-

¹⁵ <https://cran.r-project.org/>

¹⁶ Note that the PSM technique is not necessary when only one variable is used; other simpler matching methods would work as well as PSM. However, PSM allows us to test how the results change when taking other galaxy properties into account for the matching (see Table 3).

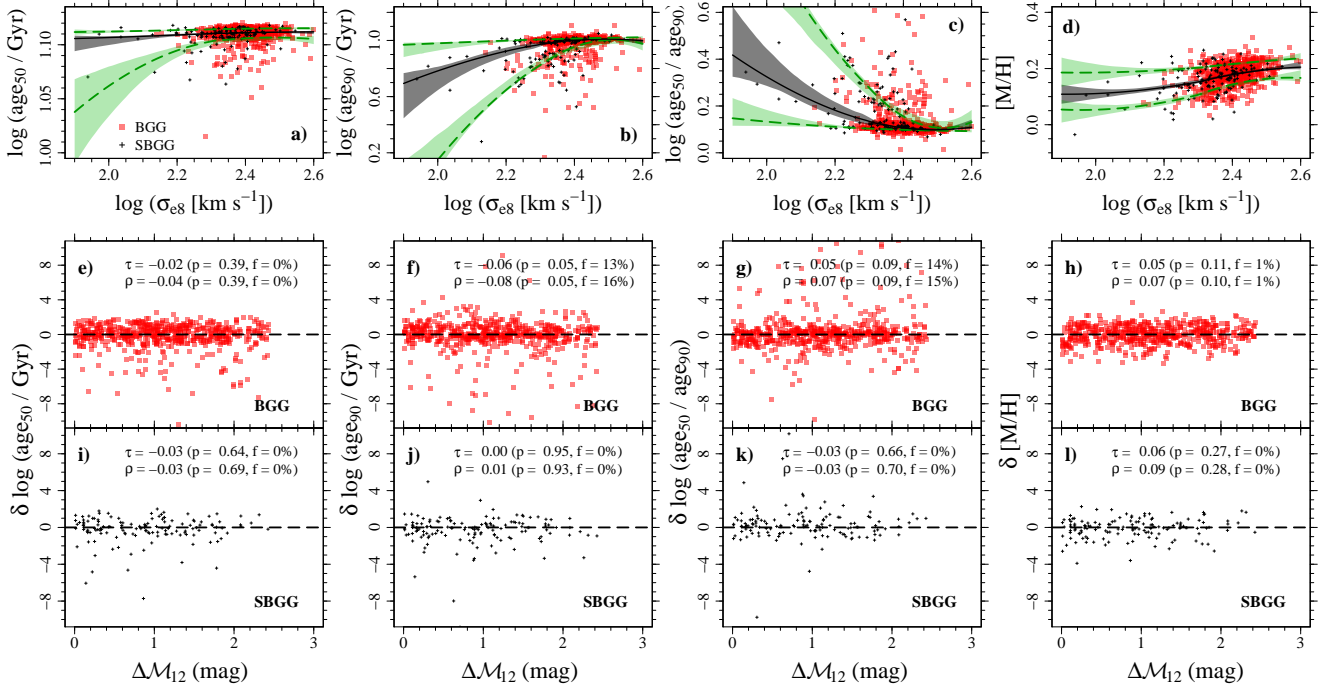


Figure 9. Same as Fig. 8 (with the same notation), but for stellar ages and metallicities obtained with the BC03 model. The upper panels (a–d) present $\log \text{age}_{50}$, $\log \text{age}_{90}$, $\log(\text{age}_{50}/\text{age}_{90})$, and metallicities as a function of $\log \sigma_{e8}$.

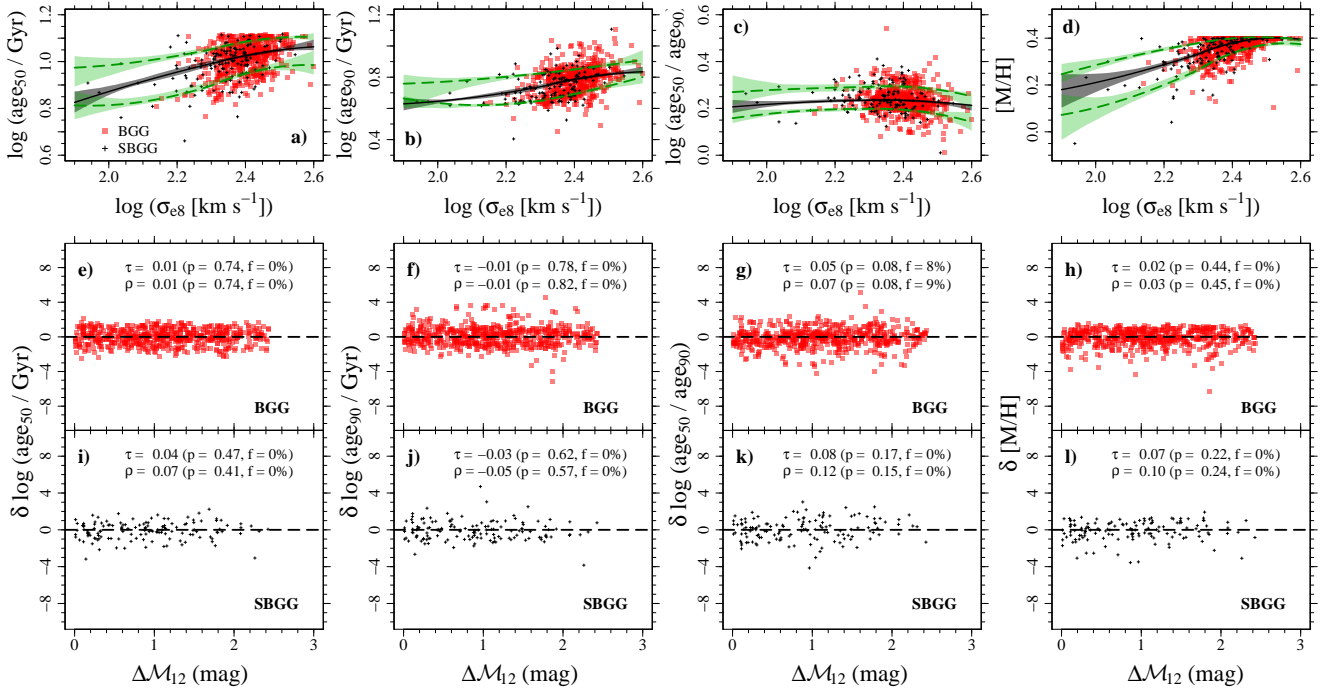


Figure 10. Same as Fig. 8, but for stellar ages and metallicities obtained with the V15 model.

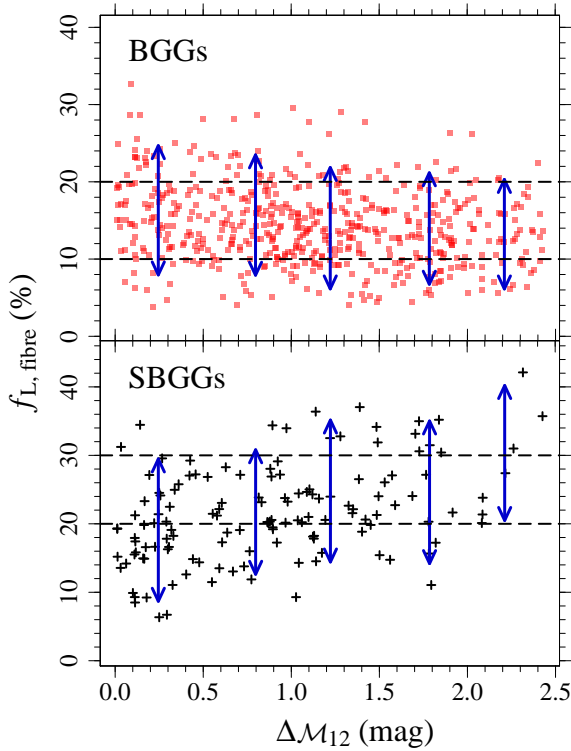


Figure 11. Fraction of Petrosian r -band light within the SDSS fibre as a function of magnitude gap. The BGGs and the elliptical SBGGs are shown in the *upper* and *lower* panels, respectively. The *blue arrows* indicate the 5th and the 95th percentiles of the $f_{L, \text{fibre}}$ distribution in bins of ΔM_{12} . The *dashed lines* indicate the $f_{L, \text{fibre}}$ limits of the subsamples defined to investigate the aperture effects (see Section 3.2.1).

pared to that of galaxies in the control sample. A KS test indicates that the shift of the distribution of SBGG R/r_{vir} to smaller radii in LGGs is significant ($p = 0.02$). The presence of a dominant BGG tends to bring the SBGGs closer in, which should lead to short times for the next merger between the BGG and the SBGG when the gap is large.

We repeated the matching by adding galaxy morphology and absolute magnitude in addition to stellar mass. As can be seen in Table 3, adding morphology and magnitude leads to similar results, i.e., there are no differences between the distribution of colour, ages, and metallicities of the SBGGs in LGGs and the control sample. On the other hand, we find an even larger difference between the radial distributions of LGG SBGGs and of the galaxies in the control sample ($p < 0.01$).

4 DISCUSSION

4.1 Stellar populations of the brightest group galaxies

As shown in Figs. 8 to 10 and in Table 1, we find no significant trends of BGG properties with gap, suggesting that all BGGs share the same stellar population properties, regardless of the magnitude gap.

The absence of significant variations of the stellar population properties with magnitude gap is in agreement with previous results, e.g. La Barbera et al. (2009), Harrison et al. (2012), and Eigenthaler & Zeilinger (2013). These authors compared the stellar

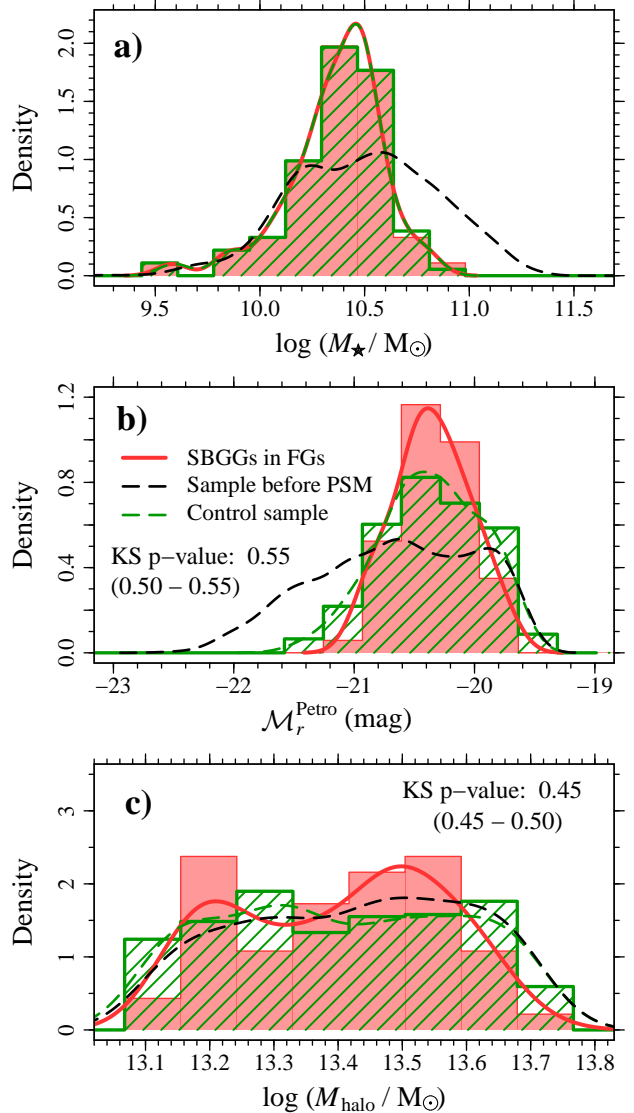


Figure 12. Stellar masses (*top*), absolute magnitudes (*middle*), and halo masses (*bottom*) before and after the PSM (see text for details). The red histograms show the distributions of $\log M_*$, M_r^{Petro} , and $\log M_{\text{halo}}$ of second-ranked galaxies in groups with $\Delta M_{12} > 2.0$ mag. The properties of the general population of galaxies in groups with $\Delta M_{12} < 2$ mag (excluding the BGGs) are indicated by the *black dashed lines*. The control sample, drawn from the sample of galaxies in groups with $\Delta M_{12} < 2$ mag by applying the PSM technique, is shown as the *green histograms*. The curves are obtained by smoothing the positions of the data points (not the histograms) using a Gaussian kernel with standard deviation equal to one third of the standard deviation of the data points. In panels **b** and **c** we indicate the p -value of the KS test (median, 1 and 99-percentiles).

populations (age, metallicities, $[\alpha/\text{Fe}]$, colours, and the radial variation of these properties) of BGGs in LGGs and normal groups, and they found no distinction between the LGGs and the control samples.

This lack of variation of SFH with magnitude gap suggests that all BGGs are formed in a very similar way, regardless of the magnitude gap. However, at a fixed halo mass, BGGs in LGGs are more massive than their counterparts in SGGs (Fig. 7a), which

Table 1. Correlation analysis of residuals of BGG properties, fit to their velocity dispersions, with magnitude gap. The results for the whole sample and for a subsample of BGGs with $10\% < f_L < 20\%$. (1) Galaxy property; (2) Kendall correlation coefficients; (3) p -values; and (4) fraction f of the 1000 realizations of the fit (see Section 2.4) that leads to $p < 0.05$. Columns (5, 6, 7) show the same for the Spearman correlation test.

| BGG property (1) | | Kendall | | | Spearman | | | |
|---|---|------------------------|-------------------|------------|------------------|-------------------|------------|------|
| | | τ (2) | p -value (3) | f (4) | ρ (5) | p -value (6) | f (7) | |
| Full sample (550 BGGs) | | | | | | | | |
| BC03 | $(g-i)$ | -0.01 ± 0.01 | 0.60 | 0.0% | -0.02 ± 0.01 | 0.57 | 0.0% | |
| | eClass | 0.02 ± 0.01 | 0.42 | 0.0% | 0.04 ± 0.01 | 0.43 | 0.0% | |
| | $\log(\text{sSFR}/\text{yr})$ | 0.00 ± 0.01 | 0.88 | 0.0% | 0.01 ± 0.01 | 0.86 | 0.0% | |
| | $[\alpha/\text{Fe}]$ | 0.02 ± 0.01 | 0.44 | 0.0% | 0.03 ± 0.01 | 0.44 | 0.0% | |
| | $\log \text{age}_{50}$ | -0.02 ± 0.01 | 0.39 | 0.0% | -0.04 ± 0.01 | 0.39 | 0.0% | |
| | $\log \text{age}_{90}$ | -0.06 ± 0.01 | 0.05 | 13.3% | -0.08 ± 0.01 | 0.05 | 15.6% | |
| | $\log(\text{age}_{50}/\text{age}_{90})$ | 0.05 ± 0.01 | 0.09 | 14.5% | 0.07 ± 0.02 | 0.09 | 14.7% | |
| | $[\text{M}/\text{H}]$ | 0.05 ± 0.01 | 0.11 | 0.7% | 0.07 ± 0.01 | 0.10 | 0.8% | |
| | V15 | $\log \text{age}_{50}$ | 0.01 ± 0.01 | 0.74 | 0.0% | 0.01 ± 0.01 | 0.74 | 0.0% |
| | | $\log \text{age}_{90}$ | -0.01 ± 0.01 | 0.78 | 0.0% | -0.01 ± 0.01 | 0.82 | 0.0% |
| $\log(\text{age}_{50}/\text{age}_{90})$ | | 0.05 ± 0.01 | 0.08 | 8.5% | 0.07 ± 0.01 | 0.08 | 9.2% | |
| $[\text{M}/\text{H}]$ | | 0.02 ± 0.01 | 0.44 | 0.4% | 0.03 ± 0.01 | 0.45 | 0.4% | |
| BGGs with $10\% < f_{\text{L}} < 20\%$ (368 BGGs) | | | | | | | | |
| BC03 | $(g-i)$ | -0.01 ± 0.01 | 0.70 | 0.0% | -0.02 ± 0.01 | 0.66 | 0.0% | |
| | eClass | 0.03 ± 0.01 | 0.34 | 0.0% | 0.05 ± 0.01 | 0.35 | 0.0% | |
| | $\log(\text{sSFR}/\text{yr})$ | 0.02 ± 0.01 | 0.61 | 0.0% | 0.03 ± 0.01 | 0.60 | 0.0% | |
| | $[\alpha/\text{Fe}]$ | 0.02 ± 0.01 | 0.54 | 0.0% | 0.03 ± 0.01 | 0.55 | 0.0% | |
| | $\log \text{age}_{50}$ | 0.01 ± 0.01 | 0.88 | 0.0% | 0.01 ± 0.02 | 0.90 | 0.0% | |
| | $\log \text{age}_{90}$ | -0.03 ± 0.01 | 0.39 | 0.0% | -0.05 ± 0.02 | 0.38 | 0.0% | |
| | $\log(\text{age}_{50}/\text{age}_{90})$ | 0.02 ± 0.01 | 0.63 | 0.0% | 0.02 ± 0.02 | 0.64 | 0.0% | |
| | $[\text{M}/\text{H}]$ | 0.03 ± 0.01 | 0.46 | 0.0% | 0.04 ± 0.01 | 0.46 | 0.0% | |
| | V15 | $\log \text{age}_{50}$ | 0.00 ± 0.01 | 0.92 | 0.0% | 0.01 ± 0.01 | 0.86 | 0.0% |
| | | $\log \text{age}_{90}$ | -0.02 ± 0.01 | 0.60 | 0.0% | -0.03 ± 0.01 | 0.63 | 0.0% |
| $\log(\text{age}_{50}/\text{age}_{90})$ | | 0.05 ± 0.01 | 0.13 | 7.2% | 0.08 ± 0.01 | 0.12 | 8.3% | |
| $[\text{M}/\text{H}]$ | | -0.02 ± 0.01 | 0.58 | 0.0% | -0.03 ± 0.02 | 0.56 | 0.0% | |

could be due to a higher star formation efficiency in LGG BGGs compared to those in SGGs. But, in this case, LGG BGGs should have higher metallicities than BGGs in SGGs, which we do not observe in our analysis once we correct for galaxy velocity dispersion. Alternatively, they may have formed the bulk of their stellar masses in an early wet merger event, which would have little effect on the traceable SFHs of these systems. Finally, LGG BGGs could have undergone more mergers than BGGs in SGGs. In this scenario, the fact that we do not observe any trend with gap of ages and metallicities implies that all BGGs would have been formed by mergers, and these mergers were dry.

The analysis by Díaz-Giménez et al. (2008) of galaxies in semi-analytical models run on the Millenium simulations show that BGGs in haloes more massive than $5 \times 10^{13} M_{\odot}$ are mainly formed by gas-poor mergers, regardless of the magnitude gap of their host haloes. The median redshift to form half of the stellar mass is $z \sim 3.5$ for central galaxies in LGGs and $z \sim 3.7$ in SGGs, which corresponds to median ages of ≈ 11.8 and 12 Gyr. However, the difference of ~ 0.2 Gyr in median age is not detectable with the time resolution of our SFH analysis.

Díaz-Giménez et al. furthermore show that, although LGGs assembled most of their virial mass at higher redshifts in comparison with SGGs, BGGs in LGGs merged later compared to their non-LGG counterparts: the last major merger in LGGs and SGGs occurred ~ 4.3 Gyr and ~ 4.7 Gyr ago (median), respectively. The stellar population synthesis (SPS) method can trace the SFHs, but not the merger history, i.e., it is possible to determine when the stars

were formed but not when they were accreted to the BGG. However, a late wet merger followed by a burst of star formation could be identified in the SFH of a galaxy. But the typical time difference between the last major mergers in LGGs vs SGGs of 0.4 Gyr at a lookback time of over 4 Gyr ago is still challenging to detect in an SPS analysis.

Our results also show that the higher M_{halo}/L_r ratios in LGGs compared to that in LGGs found in several studies (Jones et al. 2003; Yoshioka et al. 2004; Khosroshahi et al. 2007; Proctor et al. 2011) are unlikely to be due to differences in the stellar population properties. Since we find no variation of stellar population properties with gap (i.e., M_*/L_r is independent of $\Delta\mathcal{M}_{12}$) and since the halo mass-to-luminosity ratios can be written as $M_{\text{halo}}/L_r = (M_{\text{halo}}/M_*)(M_*/L_r)$, then any variation of M_{halo}/L_r with gap must be a consequence of differences in the M_*/M_{halo} ratios. Therefore, the high halo mass-luminosity ratios of LGGs can be interpreted as low M_*/M_{halo} ratios, as previously suggested. Alternatively, the halo mass-luminosity ratios of LGGs could be, in fact, no different from that of SGGs, as suggested in other studies (e.g., Voevodkin et al. 2010; Harrison et al. 2012; Girardi et al. 2014). In a forthcoming paper (Trevisan et al. 2016), we will address the M_*/L_r and the M_*/M_{halo} ratios versus gap relations in more detail.

Finally, we repeated the analysis presented in Section 3.2 using stellar masses instead of velocity dispersions, and we find no statistically significant trend of the stellar mass-corrected properties with $\Delta\mathcal{M}_{12}$ for any of the BGG and the SBGG properties. In

Table 2. Same as Table 1, but for the SBGGs.

| SBGG property (1) | Kendall | | | Spearman | | |
|--|---|-------------------|--------------|-----------------------------------|-------------------|--------------|
| | τ (2) | p -value (3) | f (4) | ρ (5) | p -value (6) | f (7) |
| Full sample (138 elliptical SBGGs) | | | | | | |
| $(g-i)$ | 0.09 ± 0.01 | 0.11 | 2.4% | 0.14 ± 0.01 | 0.11 | 1.6% |
| eClass | -0.01 ± 0.01 | 0.93 | 0.0% | -0.01 ± 0.02 | 0.92 | 0.0% |
| $\log(\text{sSFR}/\text{yr})$ | 0.13 ± 0.01 | 0.02 | 93.8% | 0.19 ± 0.02 | 0.02 | 91.3% |
| $[\alpha/\text{Fe}]$ | 0.02 ± 0.01 | 0.77 | 0.0% | 0.03 ± 0.02 | 0.75 | 0.0% |
| BC03 | $\log \text{age}_{50}$ | -0.03 ± 0.01 | 0.64 | -0.03 ± 0.02 | 0.69 | 0.0% |
| | $\log \text{age}_{90}$ | 0.00 ± 0.02 | 0.95 | 0.01 ± 0.04 | 0.93 | 0.0% |
| | $\log(\text{age}_{50}/\text{age}_{90})$ | -0.03 ± 0.03 | 0.66 | -0.03 ± 0.04 | 0.70 | 0.0% |
| | $[\text{M}/\text{H}]$ | 0.06 ± 0.01 | 0.27 | 0.09 ± 0.02 | 0.28 | 0.0% |
| V15 | $\log \text{age}_{50}$ | 0.04 ± 0.01 | 0.47 | 0.07 ± 0.02 | 0.41 | 0.0% |
| | $\log \text{age}_{90}$ | -0.03 ± 0.01 | 0.62 | -0.05 ± 0.02 | 0.57 | 0.0% |
| | $\log(\text{age}_{50}/\text{age}_{90})$ | 0.08 ± 0.01 | 0.17 | 0.12 ± 0.02 | 0.15 | 0.0% |
| | $[\text{M}/\text{H}]$ | 0.07 ± 0.01 | 0.22 | 0.10 ± 0.02 | 0.24 | 0.0% |
| SBGGs with $20\% < f_L < 30\%$ (63 elliptical SBGGs) | | | | | | |
| $(g-i)$ | 0.14 ± 0.03 | 0.11 | 18.5 | 0.18 ± 0.05 | 0.16 | 12.4 |
| eClass | -0.13 ± 0.02 | 0.14 | 4.3 | -0.17 ± 0.04 | 0.18 | 2.6 |
| $\log(\text{sSFR}/\text{yr})$ | 0.08 ± 0.02 | 0.38 | 0.0 | 0.10 ± 0.04 | 0.43 | 0.0 |
| $[\alpha/\text{Fe}]$ | 0.09 ± 0.02 | 0.32 | 0.2 | 0.12 ± 0.03 | 0.34 | 0.1 |
| BC03 | $\log \text{age}_{50}$ | 0.03 ± 0.02 | 0.76 | 0.04 ± 0.04 | 0.74 | 0.0 |
| | $\log \text{age}_{90}$ | 0.10 ± 0.03 | 0.24 | 0.16 ± 0.04 | 0.22 | 1.4 |
| | $\log(\text{age}_{50}/\text{age}_{90})$ | -0.11 ± 0.03 | 0.21 | -0.18 ± 0.05 | 0.17 | 2.9 |
| | $[\text{M}/\text{H}]$ | 0.04 ± 0.03 | 0.67 | 0.07 ± 0.05 | 0.61 | 0.1 |
| V15 | $\log \text{age}_{50}$ | 0.13 ± 0.02 | 0.14 | 0.21 ± 0.03 | 0.09 | 7.3 |
| | $\log \text{age}_{90}$ | 0.00 ± 0.03 | 0.98 | 0.02 ± 0.04 | 0.89 | 0.0 |
| | $\log(\text{age}_{50}/\text{age}_{90})$ | 0.14 ± 0.03 | 0.11 | 0.20 ± 0.04 | 0.13 | 0.2 |
| | $[\text{M}/\text{H}]$ | 0.05 ± 0.02 | 0.59 | 0.07 ± 0.04 | 0.61 | 0.0 |

addition, we fitted the properties versus $\log \sigma_{\text{e8}}$ relations using a second-order polynomial to investigate if a different fitting method affects our results. We also changed the number of bins by choosing bins of 50 galaxies instead of 100. In both cases, the resulting Kendall and Spearman correlation coefficients are very similar to those that we obtain when we fit the relations with LOESS using bins with 100 galaxies (see Section 2.4). Again, we find no significant trends of the residuals of stellar population diagnostics with magnitude gap, except, again for sSFR in SBGGs, but this trend is no longer significant (again) when we limit the range of the fraction of the luminosity within the fibre.

4.2 Projected separation between BGGs and SBGGs versus gap

The comparison between SBGGs and normal galaxies of all morphological types (Section 3.3) shows that the stellar populations of SBGGs in LGGs are statistically compatible with similar galaxies in normal groups (Figs. 13).

However, we find that SBGGs in LGGs lie significantly closer to the BGGs (in projection, Fig. 14). Dynamical friction should cause orbits to decay faster for galaxies whose subhalo masses are greater in terms of the halo (group) mass. But since our control sample was designed to have the same set of stellar masses as our LGG SBGGs, and since we found no trend of lower halo mass for the SBGG LGGs (Fig. 12c), one does not expect to have different orbital decay times. Therefore, the lower normalized radii of SBGGs in LGGs must indicate that these galaxies entered their

groups at earlier times than the similar stellar mass galaxies of the control sample.

To estimate the time of entry, one can assume that the mean density scales as r^{-2} near the group scale radius ($\sim r_{\text{vir}}/4$), and also as t^{-2} (which is correct for $\Omega_{\text{M}} = 1$ and $\Omega_{\Lambda} = 0$). Therefore, the time of entry scales roughly as the radius. According to Table 3 and Fig. 14b, the SBGGs in LGGs lie $\Delta r \sim 0.05 r_{\text{vir}}$ closer to the BGG than similar galaxies in normal groups, which means that they entered the group $\Delta t \sim \Delta r t/r$ earlier. Assuming the NFW profile at all times and that the physical density remains constant within the virial radius (see Mamon 1992), then we are able to compute the time of entry of a galaxy into a group through the relation

$$\rho_{\text{mean}}(r, t = t_0) = \rho_{\text{mean}}(r_{\text{vir}} = r, t) \quad (4)$$

which leads to solving

$$\Delta(z)H^2(z) = \Delta(z=0)H_0^2 \frac{\ln(cx+1) - [cx/(cx+1)]}{\ln(c) - [c/(c+1)]} \quad (5)$$

where $x = r/r_{\text{vir}}(z=0)$ and c is the concentration. Solving eq. (5) by shifting x by $-0.05 r_{\text{vir}}$ and comparing the results, we obtain $\Delta t = 600$ Myr.

One may wonder whether the virial radii of LGGs could have been overestimated, leading to lower R/r_{vir} values for SBGGs within these groups. However, the group masses determined by Yang et al. catalogue (hence the radii derived from them) are not expected to be biased by the magnitude gap, since the abundance matching between observed groups and the theoretical halo mass function is performed using the total group luminosity. On the other hand, if LGGs really have abnormally high M_{halo}/L_r , as suggested by many authors (Jones et al. 2003; Yoshioka et al. 2004;

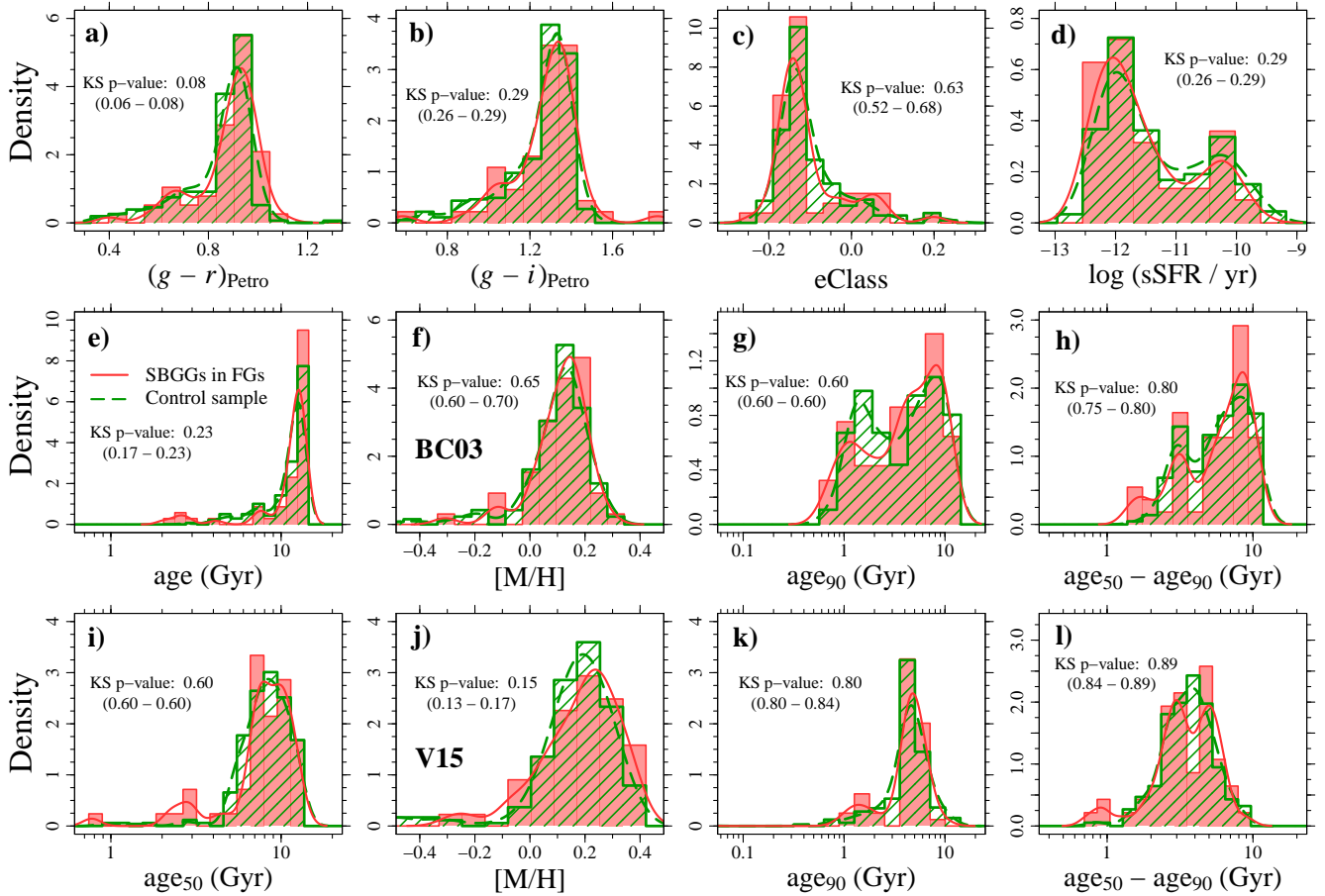


Figure 13. Comparison between the properties of second-ranked galaxies in LGGs (red) and the control sample in groups with $\Delta M_{12} < 2.0$ mag (green), described in Section 3.3. *Upper panels:* $g - r$ (a) and $g - i$ (b) colours, eClass parameters (c), and sSFR (d). Second-ranked galaxies in LGGs groups and the control sample are represented by red and green lines/histograms, respectively. *Middle and lower panels:* median ages (e, i), metallicities (f, j), lookback times when 90% of the stellar mass was formed (g, k), and elapsed time from the formation of 50% to 90% of the total stellar mass formed in the galaxy (h, l). The quantities derived from spectral modeling based on the BC03 SSP model are presented in panels e to h, and panels i to l show the results obtained with the V15 model. In each panel we indicate the p -value of the KS test (median, 1 and 99-percentiles).

Khosroshahi et al. 2007; Proctor et al. 2011; but see Voevodkin et al. 2010; Harrison et al. 2012; Girardi et al. 2014 for an alternative view), Yang et al. could have underestimated the halo masses of LGGs, since they derive halo masses from group optical luminosities with abundance matching. Therefore, the group virial radii may have been underestimated for the LGGs, and hence the normalized projected distances between the SBGGs and BGGs in LGGs may be even smaller, meaning that SBGGs in LGGs may have entered the group more than 600 Myr earlier than similar galaxies in regular groups.

If the earlier entry scenario is correct, and given the known segregation of fraction of quenched (or inversely of star-forming) galaxies (e.g., von der Linden et al. 2010; Mahajan et al. 2011), one would expect that the radial segregation of SBGG in LGGs relative to galaxies of the same stellar mass in regular groups would lead to the former having older stellar populations. Nevertheless, we do not observe any difference between the ages of LGG SBGGs and those of similar galaxies in regular groups. In addition, the fractions of star-forming galaxies ($\log[\text{sSFR}/\text{yr}] > -11$) among the LGG SBGGs and galaxies in the control sample are very similar

(25% and 34%, respectively), with Barnard’s test indicating low statistical significance ($p > 0.1$).

4.3 Fossil versus large-gap groups

In the formal definition (Jones et al. 2003), a group is classified as fossil if its bolometric X-ray luminosity is greater than $10^{42} h_{50}^{-2} \text{ erg s}^{-1}$ (in addition to the $\Delta M_{12} > 2$ mag within $0.5 r_{\text{vir}}$). Therefore, since our sample definition does not include the X-ray criteria, some of our LGGs might not be FGs¹⁷.

Fossil groups are believed to be systems that have assembled their masses at relatively early times. However, according to Raouf et al. (2014), who analyzed a semi-analytical model of galaxy formation, only a fraction of large-gap groups are in fact “old” systems, i.e., assembled at least half of their total mass at $z > 1$. Raouf et al. predict that $\sim 85\%$ of groups with $2 < \Delta M_{12} < 2.5$ and r -band luminosities between 1.9×10^{10} and $2.0 \times 10^{11} h^{-2} L_{\odot}$

¹⁷ However, we note that according to Dariush et al. (2007), groups with $\log(M_{\text{halo}}/M_{\odot}) \gtrsim 13.2$ are typically X-ray FGs.

Table 3. Comparison between SBGGs in LGGs and the control sample. We applied the Propensity Score Matching analysis using (1) $\log M_*$; (2) $\log M_*$ and $\mathcal{M}_r^{\text{Petro}}$; (3) $\log M_*$ and morphology. We show the differences between the median values (Δmedian) and the quantile-quantile distances between the distributions (**Q-Q distances**) of $\log M_*$, $\mathcal{M}_r^{\text{Petro}}$, $\log M_{\text{halo}}$, and R/r_{vir} of the LGG SBGGs and control samples. The comparison between the properties of galaxies in the two samples (**KS p-values**) and the fraction of different **morphological types** in the control sample are shown.

| | $\log M_*$ | $\log M_*$ & $\mathcal{M}_r^{\text{Petro}}$ | $\log M_*$ & morph. |
|---|---|--|------------------------|
| | (1) | (2) | (3) |
| Δmedian | | | |
| $\log(M_*/M_\odot)$ | 0.0005 | -0.006 | 0.020 |
| $\mathcal{M}_r^{\text{Petro}} (\text{mag})$ | -0.045 | 0.01 | -0.053 |
| $\log(M_{\text{halo}}/M_\odot)$ | -0.016 | -0.019 | -0.015 |
| $f_L (\%)$ | -2.05 | -2.77 | -1.57 |
| R/r_{vir} | 0.053 | 0.062 | 0.073 |
| Q-Q distances | | | |
| $\log(M_*/M_\odot)$ | -0.0003 | -0.014 | -0.0002 |
| $\mathcal{M}_r^{\text{Petro}} (\text{mag})$ | -0.0022 | 0.018 | -0.0052 |
| $\log(M_{\text{halo}}/M_\odot)$ | 0.0085 | -0.002 | 0.008 |
| $f_L (\%)$ | -1.48 | -2.53 | -1.33 |
| R/r_{vir} | 0.0425 | 0.043 | 0.052 |
| KS p-values | | | |
| $(g-r)$ | 0.08 | 0.13 | 0.07 |
| $(g-i)$ | 0.29 | 0.41 | 0.41 |
| eClass | 0.63 | 0.40 | 0.72 |
| $\log(\text{sSFR}/\text{yr})$ | 0.29 | 0.50 | 0.23 |
| BC03 | $\log \text{age}_{50}$ | 0.23 | 0.07 |
| | $\log \text{age}_{90}$ | 0.65 | 0.50 |
| | $\log(\text{age}_{50}/\text{age}_{90})$ | 0.60 | 0.29 |
| | [M/H] | 0.80 | 0.50 |
| V15 | $\log \text{age}_{50}$ | 0.60 | 0.70 |
| | $\log \text{age}_{90}$ | 0.15 | 0.11 |
| | $\log(\text{age}_{50}/\text{age}_{90})$ | 0.80 | 0.60 |
| | [M/H] | 0.89 | 0.85 |
| R/r_{vir} | 0.020 | 0.007 | 0.001 |
| Morphological types | | | |
| $f_{\text{elliptical}}$ | 8.5% | 10.9% | 9.4% |
| f_{spiral} | 25.5% | 26.4% | 20.8% |
| $f_{\text{uncertain}}$ | 65.1% | 61.8% | 69.8% |

are “old” groups. The fraction of old systems decreases to $\sim 50\%$ among high luminosity groups ($2.0 \times 10^{11} < L_r < 5.7 \times 10^{11} h^{-2} L_\odot$).

Given that 54 (91%) of our large-gap groups have luminosities $< 2 \times 10^{11} h^{-2} L_\odot$, and all of them have are less luminous than $5 \times 10^{11} h^{-2} L_\odot$, we estimate the fraction of old groups (i.e., true FGs) in our sample to be $\sim 80\%$ according to the predictions of Raouf et al.. However, since the assembly history of haloes cannot be directly observed, it is very difficult to compare predictions from simulations and observations. So, although a connection between LGGs and FGs must exist, determining the exact relation between these two classes of systems is challenging. Hence, it is not clear whether our conclusions on the lack of differences in the SFHs of BGGs and SBGGs within LGGs and SGGs may be generalized to the 1st and the 2nd-ranked galaxies in fossil vs. non-fossil groups.

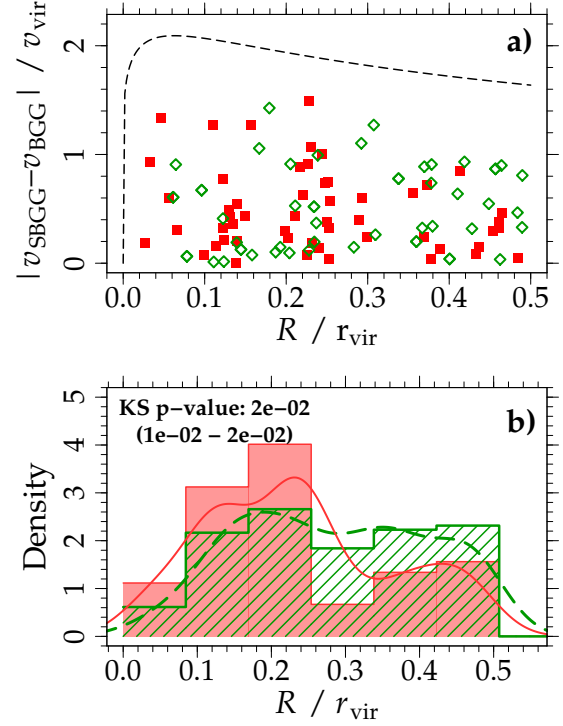


Figure 14. Diagram of $|v_{\text{los}}|/v_{200}$ vs. R/r_{vir} (upper panel) and normalized projected distance to the BGG lower panel. The second-ranked galaxies in LGGs and the control sample in groups with $\Delta M_{12} < 2.0$ mag (green), described in Section 3.3 are shown in red and green, respectively. In panel b we indicate the p-value of the KS test (median, 1st and 99th percentiles)

5 SUMMARY AND CONCLUSIONS

In this study, we used a complete sample of 550 SDSS groups to investigate how the properties and star formation histories of the BGGs (restricted to elliptical morphologies) and SBGGs vary with the magnitude gap, after removing the dependences with velocity dispersion and stellar mass. We computed galaxy median ages, the lookback times at which 90% of the total stellar mass was formed, mass-weighted metallicities, and $[\alpha/\text{Fe}]$. We also examined galaxy colours, specific star formation rates, and the eClass parameter.

While the trends of stellar populations with velocity dispersion (or stellar mass) often show major differences according to the chosen single stellar population model, several conclusions stand out, all of which are independent of the adopted spectral model:

- After correcting for trends with velocity dispersion, the BGGs follow the same distributions of $g-i$ colour, eClass values, sSFRs, $[\alpha/\text{Fe}]$ (Fig. 8e–h), ages, metallicities, and SFHs derived with both the Vazdekis et al. (2015) and the Bruzual & Charlot (2003) models (Figs. 9e–h and 10e–h), regardless of the magnitude gap of their host group. We analysed a subsample of BGGs with similar fraction of their total luminosity within the aperture of the SDSS fibre (Table 1), and still no trend of BGG properties with ΔM_{12} is observed.

- We found that elliptical SBGGs in groups with large gaps are very similar to those in small-gap groups, and the analysis of an homogeneous sample of SBGGs shows that there are no significant

trends of their properties with gap.

- Similarly, the stellar population properties of SBGGs of all morphologies in groups with $\Delta\mathcal{M}_{12} \geq 2.0$ mag are very similar to the general population of galaxies with similar stellar masses (Fig. 13).

- The projected separation between SBGGs and BGGs is smaller in groups with large gaps than galaxies with similar stellar masses and magnitudes residing in normal groups (Fig. 14). This appears to be due to the earlier entry of SBGGs within their now large-gap groups by ~ 600 Myr compared to similar galaxies in normal groups.

In a companion paper (Trevisan, Mamon & Khosroshahi 2016), we shed light on the merger histories of brightest group galaxies, thus constraining both their mass assembly histories and star formation histories.

ACKNOWLEDGMENTS

The authors thank the anonymous referee for very detailed, thoughtful, and constructive comments that led to significant improvements in our manuscript. MT acknowledges financial support from CNPq (process #204870/2014-3). MT acknowledges T. C. Moura for kindly providing us with the spectral indices measurements used to obtain our $[\alpha/\text{Fe}]$ estimates (Section 2.3.2). MT thanks the COIN collaboration (<https://asaip.psu.edu/organizations/iaa/iaa-working-group-of-cosmostatistics>) for providing the script to apply the PSM to our data. The preliminary version of the script was developed during the 2nd COIN Residence Program (<http://iaacoin.wix.com/crp2015>); more details can be found in de Souza et al. (2016). We acknowledge the use of SDSS data (<http://www.sdss.org/collaboration/credits.html>) and TOPCAT Table/VOTable Processing Software (Taylor 2005, <http://www.star.bris.ac.uk/~mbt/topcat/>).

APPENDIX A: CONVERSION FROM YANG $R_{180,M}$ TO $R_{200,C}$

The Yang et al. (2007) group catalogue provides group masses defined at the radius where the mean density is $\Delta_Y = 180$ times the mean density of the Universe, $\bar{\rho}_U(z)$, at the group redshift. Thus, at $z = 0$ and with $\Omega_{m,0} = 0.238$ adopted by Yang et al., the Yang group virial radius, $r_Y \equiv r_{\text{vir},Y}$ corresponds to a mean density of $180 \Omega_{m,0} \simeq 42.8$ times the critical density of the Universe, $\rho_{c,0} \equiv \rho_c(0)$, where

$$\rho_c(z) = \frac{3 H^2(z)}{8\pi G}. \quad (\text{A1})$$

The Yang group mean density can be written

$$\bar{\rho}_Y = 180 \bar{\rho}_U(z) = 180 \Omega_m(z) \rho_c(z) = 180 \Omega_{m,0} (1+z)^3 \rho_{c,0}. \quad (\text{A2})$$

We now define the groups at the radius r_{200} where the mean density is 200 times the critical density

$$\bar{\rho}_{200} = 200 \rho_c(z), \quad (\text{A3})$$

so that the mass within the virial radius is

$$M_{200} = 100 \frac{H^2(z) r_{200}^3}{G}. \quad (\text{A4})$$

From equations (A2) and (A3), the ratio of mean densities is

$$\frac{\bar{\rho}_Y}{\bar{\rho}_{200}} = 0.9 \Omega_{m,0} \frac{(1+z)^3}{E^2(z)}, \quad (\text{A5})$$

where $E(z) = H(z)/H_0 = \sqrt{\Omega_m^0(1+z)^3 + 1 - \Omega_m}$ for a flat Universe.

Assuming an NFW model (Navarro et al. 1996) for the mass distribution in the groups, the mean density profile can be expressed as

$$\bar{\rho}(r) = \bar{\rho}(a) \tilde{\rho}\left(\frac{r}{a}\right) = \bar{\rho}(a) \frac{\tilde{M}(r/a)}{(r/a)^3}, \quad (\text{A6})$$

where

$$\tilde{\rho}(x) = \frac{\tilde{M}(x)}{x^3} \quad (\text{A7})$$

$$\tilde{M}(x) = \frac{M(ax)}{M(a)} = \frac{\ln(x+1) - x/(x+1)}{\ln 2 - 1/2}, \quad (\text{A8})$$

with $\tilde{\rho}(1) = \tilde{M}(1) = 1$. Since the scale radius a is fixed, equations (A5) and (A6) lead to

$$\frac{\bar{\rho}_Y}{\bar{\rho}_{200}} = \frac{\tilde{\rho}(c_Y)}{\tilde{\rho}(c_{200})} = 0.9 \Omega_{m,0} \frac{(1+z)^3}{E^2(z)}, \quad (\text{A9})$$

where $c_{200} = r_{200}/a$ and $c_Y = r_Y/a$. We can use the concentration-mass relation for Λ CDM halos (that of Maccio et al. 2008), $c_{200} = c_{\Lambda\text{CDM}}(M_{200})$, and we write the Yang concentration parameter as

$$\begin{aligned} c_Y = c_{200} \frac{r_Y}{r_{200}} &= c_{\Lambda\text{CDM}}(M_{200}) \left[\left(\frac{M_Y}{M_{200}} \right) \left(\frac{\bar{\rho}_{200}}{\bar{\rho}_Y} \right) \right]^{1/3} \\ &= \frac{200}{180 \Omega_{m,0}} \frac{c_{\Lambda\text{CDM}}(M_{200}) E^{2/3}(z)}{1+z} \left(\frac{M_Y}{M_{200}} \right)^{1/3}. \end{aligned} \quad (\text{A10})$$

Combining equations (A5) and (A10), one can solve

$$\tilde{M} \left(\frac{(0.9 \Omega_m^0)^{-1/3} c_{\Lambda\text{CDM}}(M_{200}) [E^{2/3}(z)/(1+z)] (M_Y/M_{200})^{1/3}}{\tilde{M}[c_{\Lambda\text{CDM}}(M_{200})]} \right) M_{200} = M_Y \quad (\text{A11})$$

for M_{200} , where we used using equations (A7) and (A8), where the $(\ln 2 - 1/2)$ term in the latter scales out.

The virial radius r_{200} is then obtained by inverting equation (A4) to give

$$r_{200} = \left(\frac{1}{100} \frac{G M_{200}}{H_0^2} \right)^{1/3} \simeq 432 \left(\frac{M_{200}}{10^{13} M_\odot} \right) \text{ kpc} \quad (\text{A12})$$

for $H_0 = 73 \text{ km s}^{-1} \text{ Mpc}^{-1}$, as adopted by Yang et al..

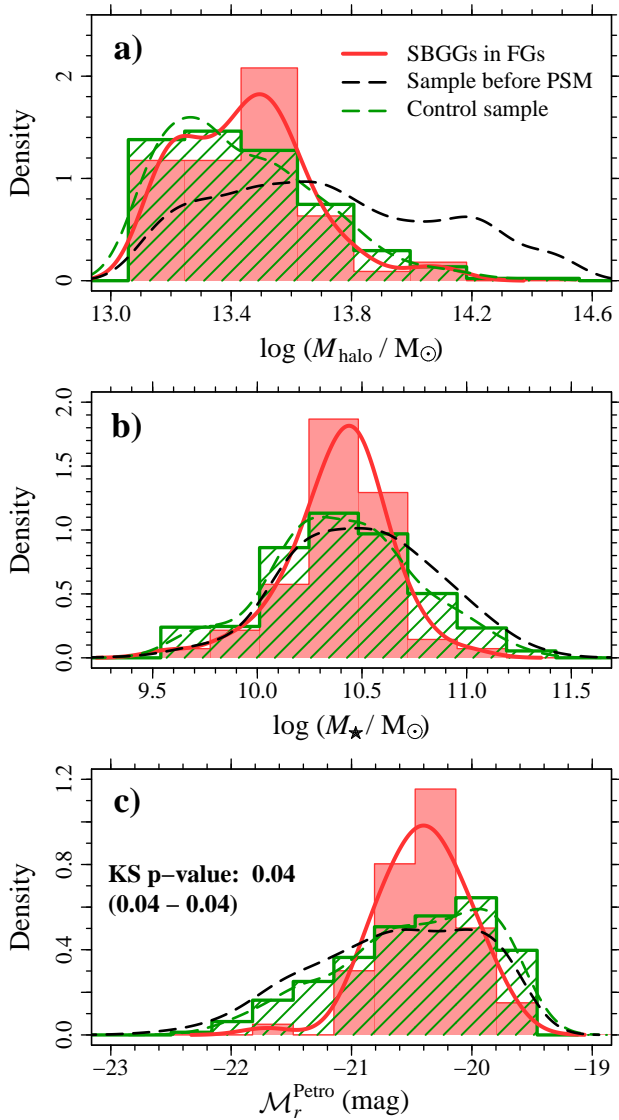


Figure B1. Halo masses (*top*), stellar masses (*middle*) and absolute magnitudes (*bottom*) before and after the PSM (see for details). The red histograms show the distributions of $\mathcal{M}_r^{\text{Petro}}$, $\log M_*$, and $\log M_{\text{halo}}$ of second-ranked galaxies in groups with $\Delta\mathcal{M}_{12} > 2.0$ mag. The properties of the general population of galaxies in groups with $\Delta\mathcal{M}_{12} < 2$ mag (excluding the BGGs) are indicated by the black histograms. The control sample, drawn from the sample of galaxies in groups with $\Delta\mathcal{M}_{12} < 2$ mag by applying the PSM technique (using both halo mass and stellar mass to perform the matching), is shown as the green histograms. The curves are obtained by smoothing the positions of the data points (not the histograms) using a Gaussian kernel with standard deviation equal to one third of the standard deviation of the data points. In panel c, we indicate the p -value of the KS test (median, 1 and 99-percentiles).

APPENDIX B: PROPENSITY SCORE MATCHING

To apply the PSM technique, we used the R package *MATCHIT* (Ho et al. 2011). The main goal is to select from the “*untreated sample*” a control sample in which the distributions of observed properties are as similar as possible to those of the “*treated sample*”. First, the propensity scores p_k (the probability that the unit k will receive

treatment) are estimated. Then, the untreated units are matched to the treated units according to a given matching algorithm.

We adopted the logistic regression approach to compute the propensity scores. Given a set \mathbf{X} of measured covariates (i.e., galaxy properties), the coefficients β are linearly fit according to the linking function defined as

$$\mathbf{Y} = \ln \left(\frac{\mu}{1 - \mu} \right), \quad (\text{B1})$$

where $Y_i = X_i\beta_i$, and the propensity scores are then given by

$$\mu = \frac{1}{1 + \exp(-\mathbf{Y})}. \quad (\text{B2})$$

We used the nearest-neighbour method to perform the matching, i.e., the treated unit i is matched to the untreated unit j in such a way that the distance $|p_i - p_j| = \min_{k \in j} \{|p_i - p_k|\}$. We allow control units to be discarded, and the model for distance measure is re-estimated after units are discarded. The match between the treated units with control units are made in random order¹⁸, and we performed the matching procedure 1000 times. In each time, we create a control sample with twice as many objects as the treated sample, and computed the KS p -values for all the galaxy properties. The values shown in Figs. 12 to 14 correspond to the median, 1, and 99-percentiles of the resulting distributions of p -values.

We first performed the match by $\log M_{\text{halo}}$ and $\log M_*$, as shown in Fig. B1. Around 48% of the galaxies in the untreated control sample reside in haloes with $\log(M_{\text{halo}}/M_{\odot}) > 13.7$ (Fig. B1a). On the other hand, only 10% of the groups with $\Delta\mathcal{M}_{12} > 2.0$ are more massive than $\log(M_{\text{halo}}/M_{\odot}) > 13.7$. As a consequence, untreated control units with $\log(M_{\text{halo}}/M_{\odot}) < 13.7$ are very likely to be matched to the treated sample, regardless of their $\log M_*$ value (i.e., the coefficient β for $\log M_{\text{halo}}$ is much greater than that for $\log M_*$), and the stellar mass becomes less important during the matching procedure. Since many studies suggest that the galaxy properties are more correlated with stellar mass than to the environment where the galaxy reside (e.g. Balogh et al. 2009; McGee et al. 2011; Trevisan et al. 2012; Woo et al. 2013, but see also Peng et al. 2010; von der Linden et al. 2010; Mahajan et al. 2011), it is desirable to get an agreement between the stellar mass distribution better than the one shown in Fig. B1b.

To overcome this issue, one option would be using the propensity score as only part of the matching distance, adding another distance to emphasise the variable of interest (E. Cameron, private communication; see also page 8 in Caliendo & Kopeinig 2008). However, the *MATCHIT* package does not include variable weighting, and implementing this approach is out of the scope of this paper. Instead, in Section 3.3, we restricted the comparison between SBGGs in LGGs and regular galaxies to groups with $\log(M_{\text{halo}}/M_{\odot}) < 13.7$, and perform the matching by galaxy properties only.

REFERENCES

- Abazajian K. N., et al., 2009, *ApJS*, **182**, 543
- Alam S., et al., 2015, *ApJS*, **219**, 12
- Balogh M. L., et al., 2009, *MNRAS*, **398**, 754
- Bernardi M., et al., 2003, *AJ*, **125**, 1849
- Blanton M. R., et al., 2003, *AJ*, **125**, 2348

¹⁸ Other two options are matching from the largest value of the distance measure to the smallest and the other way around.

- Bressan A., Fagotto F., Bertelli G., Chiosi C., 1993, *A&AS*, **100**, 647
- Brinchmann J., Charlot S., White S. D. M., Tremonti C., Kauffmann G., Heckman T., Brinkmann J., 2004, *MNRAS*, **351**, 1151
- Bruzual G., Charlot S., 2003, *MNRAS*, **344**, 1000
- Caliendo M., Kopeinig S., 2008, *Journal of Economic Surveys*, **22**, 31
- Cappellari M., et al., 2006, *MNRAS*, **366**, 1126
- Cardelli J. A., Clayton G. C., Mathis J. S., 1989, *ApJ*, **345**, 245
- Cardiel N., 2010, indexf: Line-strength Indices in Fully Calibrated FITS Spectra, Astrophysics Source Code Library (ascl:1010.046)
- Carnevali P., Cavaliere A., Santangelo P., 1981, *ApJ*, **249**, 449
- Chabrier G., 2003, *Publications of the Astronomical Society of the Pacific*, **115**, 763
- Chandrasekhar S., 1943, *ApJ*, **97**, 255
- Cid Fernandes R., Mateus A., Sodré L., Stasińska G., Gomes J. M., 2005, *MNRAS*, **358**, 363
- Colless M., et al., 2001, *MNRAS*, **328**, 1039
- D’Onghia E., Sommer-Larsen J., Romeo A. D., Burkert A., Pedersen K., Portinari L., Rasmussen J., 2005, *ApJL*, **630**, L109
- Dariush A., Khosroshahi H. G., Ponman T. J., Pearce F., Raychaudhury S., Hartley W., 2007, *MNRAS*, **382**, 433
- Dariush A. A., Raychaudhury S., Ponman T. J., Khosroshahi H. G., Benson A. J., Bower R. G., Pearce F., 2010, *MNRAS*, **405**, 1873
- Dias Pinto Vitenti S., Penna-Lima M., 2014, NumCosmo: Numerical Cosmology, Astrophysics Source Code Library (ascl:1408.013)
- Díaz-Giménez E., Muriel H., Mendes de Oliveira C., 2008, *A&A*, **490**, 965
- Dressler A., 1980, *ApJ*, **236**, 351
- Duarte M., Mamon G. A., 2015, *MNRAS*, **453**, 3848
- Dutton A. A., Macciò A. V., 2014, *MNRAS*, **441**, 3359
- Eigenthaler P., Zeilinger W. W., 2013, *A&A*, **553**, A99
- Fagotto F., Bressan A., Bertelli G., Chiosi C., 1994a, *A&AS*, **104**
- Fagotto F., Bressan A., Bertelli G., Chiosi C., 1994b, *A&AS*, **105**
- Garilli B., Maccagni D., Andreon S., 1999, *A&A*, **342**, 408
- Girardi L., Bressan A., Chiosi C., Bertelli G., Nasi E., 1996, *A&AS*, **117**, 113
- Girardi L., et al., 2014, *A&A*, **565**, A115
- Guidi G., Scannapieco C., Walcher C. J., 2015, *MNRAS*, **454**, 2381
- Harrison C. D., et al., 2012, *ApJ*, **752**, 12
- Hearin A. P., Zentner A. R., Newman J. A., Berlind A. A., 2013, *MNRAS*, **430**, 1238
- Hilbe J., 2009, Logistic regression models
- Hirschmann M., Naab T., Ostriker J. P., Forbes D. A., Duc P.-A., Davé R., Oser L., Karabal E., 2015, *MNRAS*, **449**, 528
- Ho D. E., Imai K., King G., Stuart E. A., 2011, *Journal of Statistical Software*, **42**, 1
- Jones L. R., Ponman T. J., Horton A., Babul A., Ebeling H., Burke D. J., 2003, *MNRAS*, **343**, 627
- Kauffmann G., et al., 2003, *MNRAS*, **341**, 54
- Khosroshahi H. G., Ponman T. J., Jones L. R., 2006, *MNRAS*, **372**, L68
- Khosroshahi H. G., Ponman T. J., Jones L. R., 2007, *MNRAS*, **377**, 595
- Koleva M., Prugniel P., de Rijcke S., Zeilinger W. W., 2011, *MNRAS*, **417**, 1643
- Kroupa P., 2001, *MNRAS*, **322**, 231
- Kuntschner H., 2000, *MNRAS*, **315**, 184
- La Barbera F., de Carvalho R. R., de la Rosa I. G., Sorrentino G., Gal R. R., Kohl-Moreira J. L., 2009, *AJ*, **137**, 3942
- La Barbera F., de Carvalho R. R., de la Rosa I. G., Lopes P. A. A., Kohl-Moreira J. L., Capelato H. V., 2010, *MNRAS*, **408**, 1313
- La Barbera F., Ferreras I., de Carvalho R. R., Bruzual G., Charlot S., Pasquali A., Merlin E., 2012, *MNRAS*, **426**, 2300
- La Barbera F., Ferreras I., Vazdekis A., de la Rosa I. G., de Carvalho R. R., Trevisan M., Falcón-Barroso J., Ricciardelli E., 2013, *MNRAS*, **433**, 3017
- La Barbera F., Pasquali A., Ferreras I., Gallazzi A., de Carvalho R. R., de la Rosa I. G., 2014, *MNRAS*, **445**, 1977
- Le Borgne J.-F., et al., 2003, *A&A*, **402**, 433
- Lintott C., et al., 2011, *MNRAS*, **410**, 166
- Mahajan S., Mamon G. A., Raychaudhury S., 2011, *MNRAS*, **416**, 2882
- Mamon G. A., 1987, *ApJ*, **321**, 622
- Mamon G. A., 1992, *ApJL*, **401**, L3
- Mamon G. A., Łokas E. L., 2005, *MNRAS*, **363**, 705
- Mamon G. A., Biviano A., Murante G., 2010, *A&A*, **520**, A30
- Matteucci F., Recchi S., 2001, *apj*, **558**, 351
- Matteucci F., Tornambe A., 1987, *A&A*, **185**, 51
- McGee S. L., Balogh M. L., Wilman D. J., Bower R. G., Mulchaey J. S., Parker L. C., Oemler A., 2011, *MNRAS*, **413**, 996
- Mulchaey J. S., Zabludoff A. I., 1999, *ApJ*, **514**, 133
- Navarro J. F., Frenk C. S., White S. D. M., 1996, *ApJ*, **462**, 563
- Oemler Jr. A., 1974, *ApJ*, **194**, 1
- Peng Y.-j., et al., 2010, *ApJ*, **721**, 193
- Pietrinferni A., Cassisi S., Salaris M., Castelli F., 2004, *ApJ*, **612**, 168
- Pietrinferni A., Cassisi S., Salaris M., Castelli F., 2006, *ApJ*, **642**, 797
- Pilkington K., et al., 2012, *A&A*, **540**, A56
- Ponman T. J., Allan D. J., Jones L. R., Merrifield M., McHardy I. M., Lehto H. J., Luppino G. A., 1994, *Nature*, **369**, 462
- Proctor R. N., de Oliveira C. M., Dupke R., de Oliveira R. L., Cypriano E. S., Miller E. D., Rykoff E., 2011, *MNRAS*, **418**, 2054
- R Core Team 2015, R: A Language and Environment for Statistical Computing. R Foundation for Statistical Computing, Vienna, Austria, <https://www.R-project.org>
- Raouf M., Khosroshahi H. G., Ponman T. J., Dariush A. A., Molaeinezhad A., Tavasoli S., 2014, *MNRAS*, **442**, 1578
- Rosenbaum P. R., Rubin D. B., 1983, *Biometrika*, **70**, 41
- Salim S., et al., 2007, *ApJS*, **173**, 267
- Sánchez-Blázquez P., et al., 2006, *MNRAS*, **371**, 703
- Sánchez S. F., Pérez E., Rosales-Ortega F. F., Miralles-Caballero D., López-Sánchez A. R., et al. 2015, *A&A*, **574**, A47
- Saunders W., et al., 2000, *MNRAS*, **317**, 55
- Schneider D. P., Gunn J. E., 1982, *ApJ*, **263**, 14
- Strauss M. A., Weinberg D. H., Lupton R. H., Narayanan V. K., Annis et al. 2002, *AJ*, **124**, 1810
- Taylor M. B., 2005, in Shopbell P., Britton M., Ebert R., eds, *Astronomical Society of the Pacific Conference Series Vol. 347, Astronomical Data Analysis Software and Systems XIV*, p. 29
- Thomas D., Greggio L., Bender R., 1999, *mnras*, **302**, 537
- Thomas D., Maraston C., Bender R., 2003, *MNRAS*, **339**, 897
- Thomas D., Maraston C., Bender R., Mendes de Oliveira C., 2005, *ApJ*, **621**, 673
- Thomas D., Maraston C., Johansson J., 2011, *MNRAS*, **412**, 2183
- Tinsley B. M., 1979, *ApJ*, **229**, 1046
- Trevisan M., Ferreras I., de la Rosa I. G., La Barbera F., de Carvalho R. R., 2012, *ApJL*, **752**, L27
- Trevisan M., Mamon G. A., Khosroshahi H. G., 2016, to be submitted
- Vazdekis A., Sánchez-Blázquez P., Falcón-Barroso J., Cenarro A. J., Beasley M. A., Cardiel N., Gorgas J., Peletier R. F., 2010, *MNRAS*, **404**, 1639
- Vazdekis A., et al., 2015, *MNRAS*, **449**, 1177
- Voevodkin A., Borozdin K., Heitmann K., Habib S., Vikhlinin A., Mescheryakov A., Hornstrup A., Burenin R., 2010, *ApJ*, **708**, 1376
- Walcher C. J., Coelho P. R. T., Gallazzi A., Bruzual G., Charlot S., Chiappini C., 2015, *A&A*, **582**, A46
- Weinmann S. M., van den Bosch F. C., Yang X., Mo H. J., 2006, *MNRAS*, **366**, 2
- White S. D. M., 1976, *MNRAS*, **174**, 19
- Woo J., et al., 2013, *MNRAS*, **428**, 3306
- Yang X., Mo H. J., van den Bosch F. C., Pasquali A., Li C., Barden M., 2007, *ApJ*, **671**, 153
- Yip C. W., et al., 2004, *AJ*, **128**, 585
- Yoshioka T., Furuzawa A., Takahashi S., Tawara Y., Sato S., Yamashita K., Kumai Y., 2004, *Advances in Space Research*, **34**, 2525
- de la Rosa I. G., La Barbera F., Ferreras I., de Carvalho R. R., 2011, *MNRAS*, **418**, L74
- de Souza R. S., et al., 2015, *Astronomy and Computing*, **12**, 21
- de Souza R. S., et al., 2016, *MNRAS*, **461**, 2115
- de Vaucouleurs G., de Vaucouleurs A., Corwin Jr. H. G., Buta R. J., Paturel G., Fouqué P., 1991, *Third Reference Catalogue of Bright Galaxies*. Volume I: Explanations and references. Volume II: Data for galaxies

between 0^h and 12^h . Volume III: Data for galaxies between 12^h and 24^h .

de la Rosa I. G., de Carvalho R. R., Vazdekis A., Barbuy B., 2007, [AJ](#), **133**, 330

van den Bosch F. C., et al., 2007, [MNRAS](#), **376**, 841

von der Linden A., Wild V., Kauffmann G., White S. D. M., Weinmann S., 2010, [MNRAS](#), **404**, 1231